Journal of Applied Geophysics 90 (2013) 1–18

Contents lists available at SciVerse ScienceDirect

Journal of Applied Geophysics

journal homepage: www.elsevier.com/locate/jappgeo

Scaling behavior and the effects of heterogeneity on shallow seismic imaging of mineral deposits: A case study from Brunswick No. 6 mining area, Canada

Saeid Cheraghi [a,*], Alireza Malehmir [a], Gilles Bellefleur [b], Emmanuel Bongajum [c], Mehrdad Bastani [d]

[a] Department of Earth Sciences, Uppsala University, SE 75236 Uppsala-Sweden
[b] Geological Survey of Canada, Ottawa, 615 Booth St. K1A0E9 Ontario, Canada
[c] University of Alberta, Edmonton, Alberta, Canada T6G2E1
[d] Geological Survey of Sweden, Box 670, SE75128, Uppsala, Sweden

ARTICLE INFO

Article history:
Received 17 July 2012
Accepted 11 December 2012
Available online 22 December 2012

Keywords:
Crystalline rock
Scattering
Heterogeneity
Scaling
Modeling

ABSTRACT

We have studied the scaling behavior of compressional-wave velocity and density logs from an exploration borehole that extends down to about 700 m depth in the Brunswick No. 6 mining area, Bathurst Mining Camp, Canada. Using statistical methods, vertical and horizontal scale lengths of heterogeneity were estimated. Vertical scale length estimates from the velocity, density and calculated acoustic impedance are 14 m, 33 m, and about 20 m, respectively. Although the estimated scale length for the acoustic impedance implies a weak scattering environment, elastic finite difference modeling of seismic wave propagation in 2D heterogeneous media demonstrates that even this weak scattering medium can mask seismic signals from small, but yet economically feasible, massive sulfide deposits. Further analysis of the synthetic seismic data suggests that in the presence of heterogeneity, lenticular-shaped targets may only exhibit incomplete diffraction signals whereby the down-dip tails of these diffractions are mainly visible on the stacked sections. Therefore, identification of orebody generated diffractions is much easier on the unmigrated stacked sections than on migrated stacked sections. The numerical seismic modeling in 2D heterogeneous media indicates that in the presence of large horizontal, but small vertical scale lengths (structural anisotropy), identification of massive sulfide deposits is possible, but their delineation at depth requires detailed velocity modeling and processing algorithms which can handle the anisotropy.

1. Introduction

Application of 2D and 3D reflection seismic methods for mineral exploration in crystalline rocks dates back to more than 20 years ago (Malehmir et al., 2012 and references therein; Milkereit et al., 1996, 2000; Pretorius et al., 2003 and references therein). Despite the progress made during this time, the complex geology in the crystalline environment still represents a significant challenge for these methods. Distinguishing high amplitude signals from mineralization zones from that of their host rocks is an example of one of the challenges (e.g., Adam et al., 2000, 2003; Dehghannejad et al., 2010; Ehsan et al., 2012; Malehmir and Bellefleur, 2009; Malehmir et al., 2011; White et al., 2012). Most studies related to direct orebody detection have so far focused on diffracted signals generated by mineralization zones (e.g., Bellefleur et al., 2012; Bohlen et al., 2003; Dehghannejad et al., 2012; Eaton, 1999; Malehmir and Bellefleur, 2009; Malinowski et al., 2012; White et al., 2012), neglecting effects from the host rocks. However, the Earth is a heterogeneous medium (Frankel and Clayton, 1986) and several studies suggest that the general low impedance contrast in the crystalline environment combined with scattering of seismic waves from strongly deformed, metamorphosed, and heterogeneous host rocks can mask seismic signals from mineralization zones that are often small and isolated bodies (e.g., Eaton, 1999; Malehmir and Bellefleur, 2009; Milkereit and Eaton, 1998; Milkereit et al., 2000).

Very often, the heterogeneity within the earth is studied assuming a statistically random media (Frankel and Clayton, 1986; Korn, 1993; Muller et al., 1992; Roth and Korn, 1993). Such a statistical approach with the accompanying parameterization provide an effective way to generate heterogeneous models that can be used to study seismic wave propagation and seismic scattering (e.g., Bean et al., 1999; Goff and Levander, 1996; Holliger, 1996; Holliger et al., 1993, 1994; Hurich, 1996; Levander et al., 1994; Poppeliers, 2007; Wu and Aki, 1985a,b, 1988). A common statistical approach to estimate the heterogeneity of a medium is to use borehole petrophysical measurements. Such measurements allow the estimation of the fractal dimension or stochastic properties of the medium and can also provide information on the scale of the heterogeneity of various petrophysical properties such as P- and S-wave velocity and density (e.g., Bansal et al., 2010;

* Corresponding author. Tel.: +46 18 4717161; fax: +46 18 501110.
E-mail addresses: saeid.cheraghi@geo.uu.se (S. Cheraghi), alireza.malehmir@geo.uu.se (A. Malehmir), gbellefl@nrcan-rncan.gc.ca (G. Bellefleur), bongajum@ualberta.ca (E. Bongajum), mehrdad.bastani@sgu.se (M. Bastani).

0926-9851/$ – see front matter © 2012 Elsevier B.V. All rights reserved.
http://dx.doi.org/10.1016/j.jappgeo.2012.12.003

Dolan and Bean, 1997; Goff and Holliger, 1999; Kneib, 1995; Marsan and Bean, 1999; Pilkington and Todoeschuck, 2004; Wu et al., 1994). Borehole logs also help to link the statistical properties of the seismic velocity and the geological structures of exploration areas (Hurich and Kocurko, 2000; Line et al., 1998; Pullammanappallil et al., 1997). When combined with numerical modeling, the statistical properties of the medium, and the models derived from them, can help to study the effects of heterogeneity on seismic imaging of specific targets (e.g., Carpentier and Roy-Chowdhury, 2009; Frenje and Juhlin, 2000; Holliger, 1997; Holliger et al., 1996; Hurich and Kocurko, 2000; Korn, 1993). Moreover, a better understanding of the effects of heterogeneity on seismic wave propagation may allow better survey designs and processing approaches to be implemented, and result in more efficient mineral exploration strategies using reflection seismic methods (Bongajum et al., 2012; L'Heureux et al., 2009).

Although elastic finite-difference (FD) modeling has been used previously to explain the effects of the shape and composition of ore deposits (e.g., Bellefleur et al., 2012; Bohlen et al., 2003; Eaton, 1999; Malehmir et al., 2009), only a few FD studies have considered the effects of the medium heterogeneity in the modeling (e.g., Bongajum et al., 2012; L'Heureux et al., 2009). L'Heureux et al. (2009) investigated the effects of heterogeneity and resulting scattering on the seismic imaging of deep mineral deposits. They showed that the shape and size of the targets combined with the seismic scattering effects from the heterogeneous host rock are the main factors controlling the detection and delineation of massive sulfide deposits in the crystalline environment. Bongajum et al. (2012) studied the seismic scattering effects of the dip component of heterogeneous geological structures in the crystalline environment using a subsurface shot and receiver geometry. Their study suggested that the seismic scattering should not cause significant location errors, especially when longer travel paths are used for the imaging. It is evident that the crustal heterogeneity is still an open subject and more studies are required to unravel ambiguities and improve crystalline rock seismic exploration (L'Heureux et al., 2009).

In this study, we investigate the effects of heterogeneity over the Brunswick No. 6 mining area in the Bathurst Mining Camp northwest New Brunswick, Canada (Fig. 1). Both 2D and 3D seismic data are available from the study area. Although the study area is highly prospective, neither the 2D data (Cheraghi et al., 2011; Malehmir and Bellefleur, 2010) nor the 3D data (Cheraghi et al., 2012) showed strong seismic anomalies that could potentially be associated with deep mineralization. This motivated us to study the effects of heterogeneity in the host rock and its potential contributions to obscuring seismic images of any deep mineralized zones. Therefore, our aims in this study are (1) to evaluate the scaling behavior of borehole sonic and density data and to estimate scale lengths which may statistically be representative of the heterogeneity in the study area, (2) to use the estimated horizontal and vertical scale lengths for generating 2D heterogeneous petrophysical models of the compressional- and shear-wave velocities, as well as density, in the study area, and (3) to study the seismic response of some specific geometrical shapes (e.g., circle and ellipse) of targets within the 2D heterogeneous models using 2D elastic FD modeling. In addition, we also investigate the effects of source frequency, scale length and variation in the heterogeneity on imaging mineral deposits by varying these parameters.

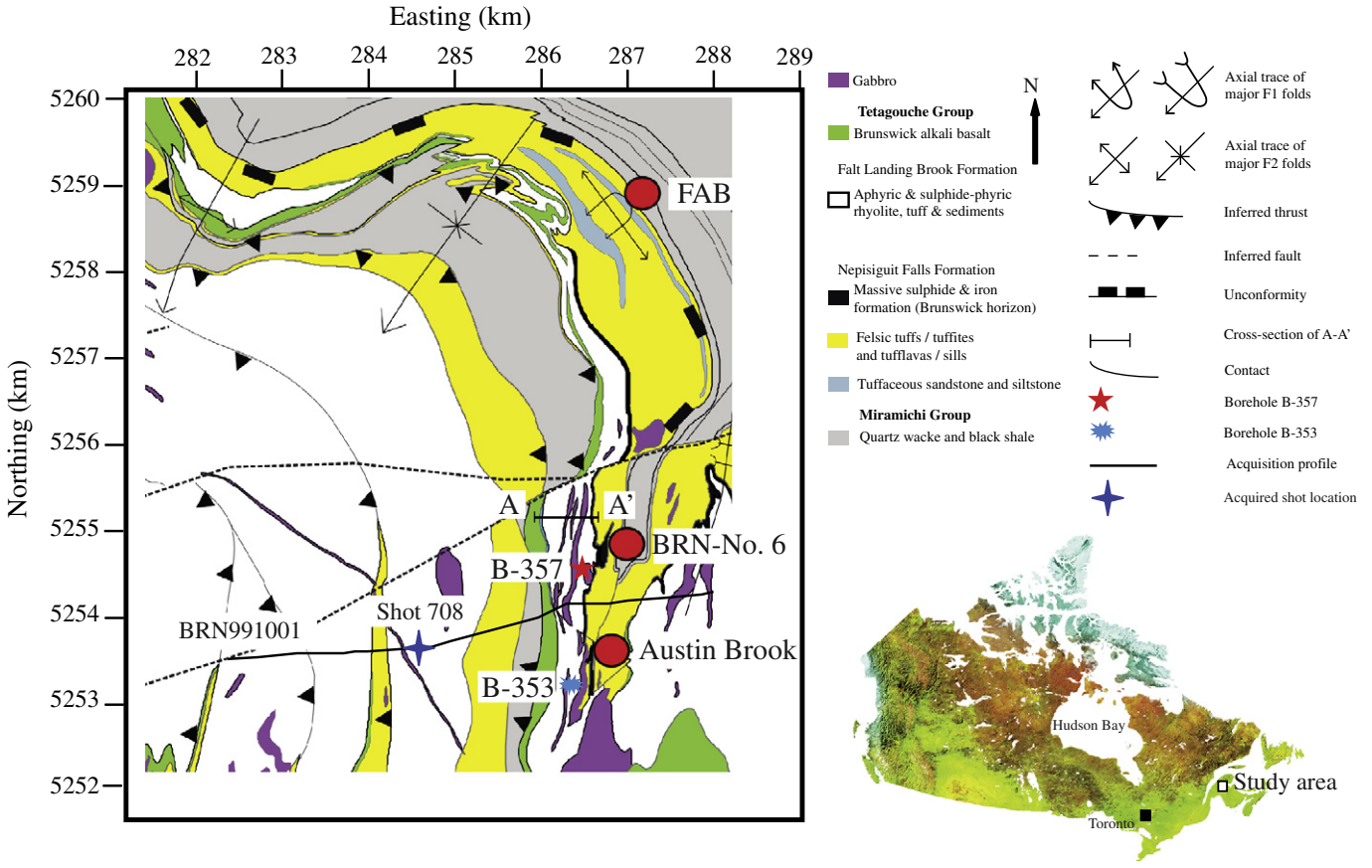

Fig. 1. Geological map of the Brunswick No. 6 mining area, Bathurst Camp, New Brunswick (modified from van Staal et al., 2003) showing location of major mineral deposits (e.g., FAB, Austin Brook and Brunswick No. 6). A–A′ is a geological cross-section shown later in this paper. Boreholes B-353 and B-357 are discussed in this paper. Shot 708 from BRN991001 2D line is shown and will be discussed later in the paper.

2. Geological setting and petrophysical data

The Brunswick No. 6 mining area is located approximately 27 km southwest of the city of Bathurst, in the Bathurst Mining Camp (van Staal, 1994; van Staal et al., 2003), New Brunswick, Canada. The Bathurst Mining Camp has been a major base metal producing area in Canada. The Brunswick No. 6 mine, the focus of this study, produced 12.2 Mt of sulfide ore from shallow depths, grading 5.43 wt.% Zn, 2.15 wt.% Pb, 0.40 wt.% Cu, and 67 g/t Ag (Luff, 1995; Wills et al., 2006). In the Brunswick No. 6 area, the oldest rocks belong to the Miramichi Group, a Cambro-Ordovician clastic metasedimentary sequence (van Staal et al., 2003). These rocks are overlain by the middle Ordovician bimodal volcanic and sedimentary rocks of the Tetagouche Group that formed within the Tetagouche-Exploits back-arc basin (Rogers and van Staal, 1997; van Staal, 1987, 1994; van Staal et al., 2003; Whalen et al., 1998), and host the VHMS (volcanic-hosted massive sulfide) and iron deposits found in the Brunswick horizon. Iron formation in the Brunswick horizon includes a mixture of sulfide, carbonate, oxide, and silicate facies. This horizon is a key target for geophysical and geochemical exploration in the camp (Gross and McLeod, 1980). The lower part of the Tetagouche Group consists of dominantly felsic volcanic and volcanoclastic rocks of the Nepisiguit Falls Formation, which are overlain by the younger rhyolite flows and rhyolitic volcanic/hyaloclastic rocks of the Flat Landing Brook Formation (Rogers et al., 2003). The youngest part of the Tetagouche Group consists of alkali basalt flows and associated clastic and exhalative sedimentary rocks of the Little River Formation (Fig. 1).

Several geological boreholes are available from the study area and provide good understanding of the subsurface geology, especially at shallow depths (Lentz and McCutcheon, 2006; Wills et al., 2006). However, only two boreholes have been logged for compressional velocity (Vp) and density (boreholes B-353 and B-357 in Fig. 1). Fig. 2 shows lithology, Vp, and density logs for these two boreholes. The sampling interval is 5 cm and 20 cm for boreholes B-353 (about 700 m deep) and B-357 (about 520 m deep), respectively. The acoustic impedance, the reflection coefficients, as well as synthetic traces (assuming sufficient lateral continuity) obtained by convolving the reflection coefficients with a 70 Hz Ricker wavelet, also are also shown in Fig. 2 (see Malehmir and Bellefleur, 2010). Since borehole B-353 is deeper and the sampling interval is shorter (allowing for more resolution), we studied the scaling behavior of the seismic velocity and density from this borehole. The density logs from both boreholes (Fig. 2) show a mean value of about 2700 kg/m^3. The Nepisiguit Falls Formation and the Flat Landing Brook Formation exhibit density variations close to the mean value (Fig. 2). The density of the massive sulfide and gabbro formations are 3400 kg/m^3 and 3000 kg/m^3, respectively. The mean value of Vp is approximately 5650 m/s, close to the values observed for the Nepisiguit Falls Formation and the Flat Landing Brook Formation (Fig. 2). Massive sulfides (Brunswick horizon) and gabbros have mean seismic velocities of about 6400 m/s. Fig. 3 shows the density cross plotted against velocity for different geological formations measured in borehole B-353. The Brunswick horizon shows the largest acoustic impedances, but with significant overlap with gabbros. The Flat Landing Brook Formation shows the lowest acoustic impedance. Therefore, in favorable conditions, both massive sulfide deposits and gabbroic bodies should produce detectable seismic signals when in contact with the Nepisiguit Falls Formation or the Flat Landing Brook Formation. From a detection perspective, massive sulfide deposits should be detected with seismic methods, but will be difficult, if not impossible, to distinguish from bodies of gabbroic composition (see also Bellefleur et al., 2012).

3. Scaling behavior of petrophysical logs

The heterogeneous nature of the Earth portrays different physical and chemical properties at various spatial locations. Wu (1989) showed that different scales of heterogeneity in the horizontal and vertical directions have direct effects on wave propagation and scattering from subsurface geological formations. Borehole petrophysical measurements provide information on the variation of any given property with depth, for example in this study Vp or density. Evaluation of the power spectrum of this variation provides information on the scaling behavior or cyclicity of these properties. Different studies have shown that over a wide range of frequencies, f, the power spectrum of a measured petrophysical property decays as $1/f^{0.5-1.5}$, that is $1/f$ flicker noise (e.g., Bean, 1996; Holliger and Goff, 2003). Fig. 4 shows calculated power spectrum for the density and Vp logs of borehole B-353. The absolute value of the slopes of the best-fitted lines to the density and Vp data are 0.8865 and 1.1570, respectively. These values are within the range of the flicker noise described above (i.e., between 0.5 and 1.5). The observed values for the slopes of the power spectrum of the density and Vp logs show that their scaling varies from a few centimeters to hundreds of meters, a matter that will be further analyzed in this study.

4. Estimating scale length

Petrophysical logs can be considered as data series comprising a general trend and a zero-mean stochastic part (Goff and Holliger, 1999; Holliger et al., 1996). The general trend can affect the estimation of the statistical parameters of petrophysical measurements and should be removed from the data prior to the estimation of the scale length (Priestly, 1981). After removing the general trend, the residual values are assumed to represent the small-scale stochastic part of the data series, which can be used to calculate the scale length of the heterogeneity. Several methods have been proposed to de-trend the data. Holliger (1997) and Holliger et al. (1996) considered the general increase in seismic velocity with depth (burial pressure) as the general trend and removed it with a best-fitting line. Goff and Holliger (1999) considered lithological and depth related fluctuations for the general trend removal; for example, they considered a binary lithology, including gneiss and metabasite, in the KTB main borehole (Germany). This approach was used because gneiss and metabasite showed two separate trends, both having increasing velocity with depth (higher velocities were observed for metabasite). Midpoints between the two trends were used to define the general trend. For borehole B-353, we calculated the best-fitting line for both density and velocity measurements (Fig. 5a and d). While there are different approaches to find the trend in the data (e.g., linear or curved), for simplicity and avoiding the addition of an interpretive bias, we estimated the trends using a straight line. Prior to the de-trending, both the density and velocity data were median-filtered to remove any spikes from the calculation. Surprisingly, the estimated trend for both density and velocity decreases with depth. Thus, the trends observed in B-353 are not consistent with increasing burial pressure and most likely result from the lithological variations in the area. The data obtained after the removal of the general trend of Vp and density values (Fig. 5b and e) define the small-scale stochastic component of the measured logs. The stochastic component of the data can now be evaluated with second-order statistical properties (i.e., autocovariance). The autocovariance is compared with the autocovariance of a predefined (theoretical) function. In our case, we selected the von Karman function as it is often used as a tool for the stochastic modeling of a wide range of random geophysical data, including borehole petrophysical data (Bongajum et al., 2012; Goff and Holliger, 1994; Goff and Jordan, 1988; Holliger et al., 1996; L'Heureux et al., 2009). The general form of the von Karman autocovariance function (von Karman, 1948) in 3-dimension is:

$$c(r) = \frac{r^{\nu} k_{\nu}(r)}{2^{\nu-1}\Gamma(\nu)}, \quad r = \sqrt{\left(\frac{x}{a_x}\right)^2 + \left(\frac{y}{a_y}\right)^2 + \left(\frac{z}{a_z}\right)^2}, \tag{1}$$

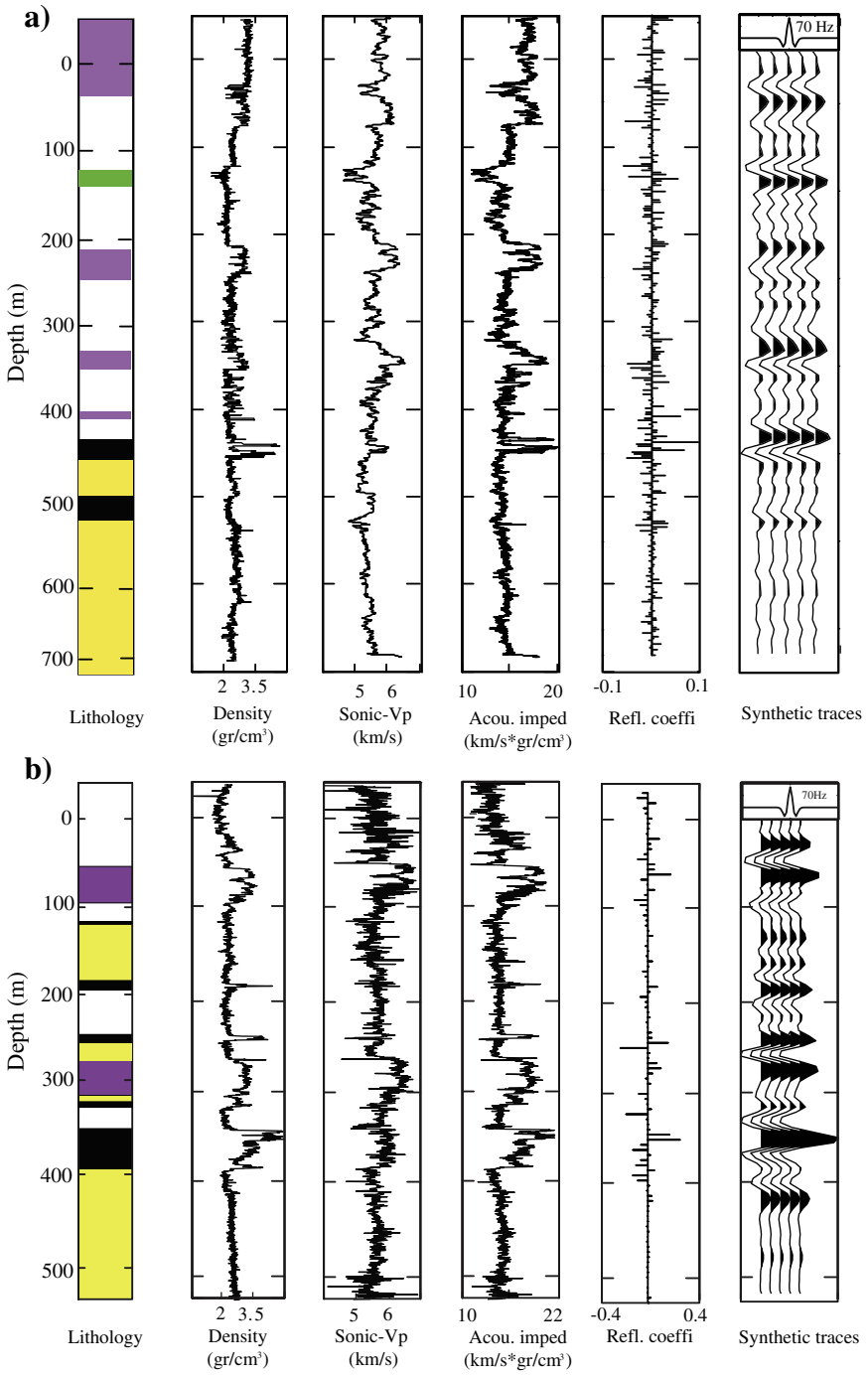

Fig. 2. Density, compressional-wave velocity (Vp), calculated acoustic impedance, reflection coefficient, and synthetic seismogram produced using a central frequency of 70 Hz. Logs are from borehole geophysical measurements in (a) B-353, and (b) B-357 (from Cheraghi et al., 2011; Malehmir and Bellefleur, 2010). Color for lithologies is the same as in Fig. 1. (For interpretation of the references to color in this figure legend, the reader is referred to the web version of the article.)

where $c(r)$ is the von Karman autocovariance function, r is the lag, ν is Hurst number, $k_\nu(r)$ is the modified second-order Bessel function, $\Gamma(\nu)$ is the gamma function, x, y, and z are spatial locations, and a_x, a_y, and a_z are scale lengths of heterogeneity in two horizontal directions and the vertical direction, respectively. By comparing the 1D (z direction) von Karman autocovariance function with the autocovariance graph of the measured property and finding the best fitting line to the measured values in a least-squares sense, the maximum scale length at which the stochastic environment remains fractal can be calculated (Goff and Jordan, 1988; Holliger, 1996). Since boreholes in the Brunswick area are relatively steep, the scale length obtained from borehole petrophysical data is assumed to represent the vertical scale length. Fig. 5c and f shows the autocovariance of the stochastic component of the density and Vp logs and the best fitting von Karman autocovariance function for each property, respectively. The calculated Hurst number (ν) and vertical scale length for the density log are 0.2165 and 33.6749 m, respectively (Fig. 5c), whereas the Hurst number (ν) and vertical scale length (a_z) for the Vp log are 0.3365 and 14.0430 m, respectively (see Fig. 5f). Table 1 summarizes the estimated statistical values.

We also estimated the vertical scale length and Hurst number for the acoustic impedance calculated from the density and sonic logs. The general trend was similarly estimated using a best-fitting straight line (Fig. 6a). To further investigate the effect of lithology on the trend, we

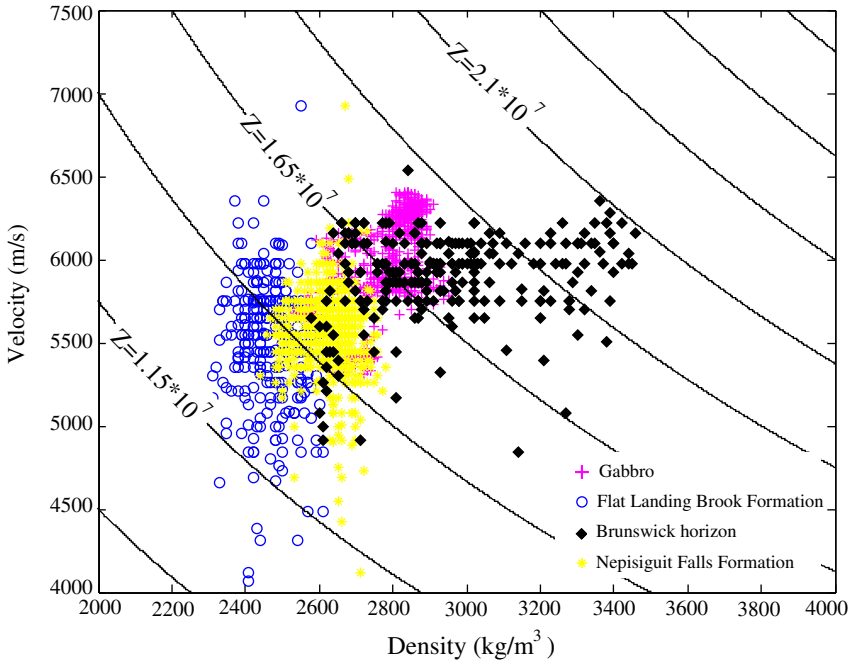

Fig. 3. Density versus velocity graph from borehole measurements (see Fig. 2a). Contours represent lines of constant acoustic impedance (SI units). It is clear that massive sulfide deposits (Brunswick horizon) have a strong contrast against their host rocks.

calculated the average acoustic impedance within each geological formation and then estimated the best linear fit to those points (Fig. 6a). The actual trend remained similar to that estimated from the entire data (Fig. 6a). After removing the general trend (estimated from the entire data set), we obtained a Hurst number (ν) of 0.4986 and a vertical scale length (a_z) of 19.5914 m, respectively (Table 1). As expected, the estimated scale length for the acoustic impedance is larger than that estimated for the Vp data and much smaller than that estimated for the density. However, the Hurst number estimated from the acoustic impedances is larger than Hurst numbers for the velocity and density (Table 1). A larger Hurst number represents a decrease in the level of small-scale heterogeneities (Korn, 1993). Since the density and Vp logs do not track each other, we think the Hurst number and the scale length calculated from the acoustic impedance may be a better representation of the statistical parameters of the stochastic environment of the Brunswick No. 6 area.

Due to the vertical nature of boreholes B-353 and B-357 the logging data from these boreholes cannot be used to estimate the horizontal scale length. Wu et al. (1994) showed a different method to calculate horizontal scale length from borehole logs. They computed a 1D von Karman autocovariance function fit to the cross-correlation graph of two the deep boreholes at the KTB site and obtained a horizontal scale length (a_x) of 3600 m, much larger than the 200 m distance between the two boreholes. In the case of the Brunswick No. 6 borehole data, the distance between the two boreholes (i.e., B-353 and B-357) is about 2000 m. We calculated the cross-correlation, but did not observe any reasonable fit to the von Karman function. This implies that the horizontal scale length is less than the distance between the two boreholes,

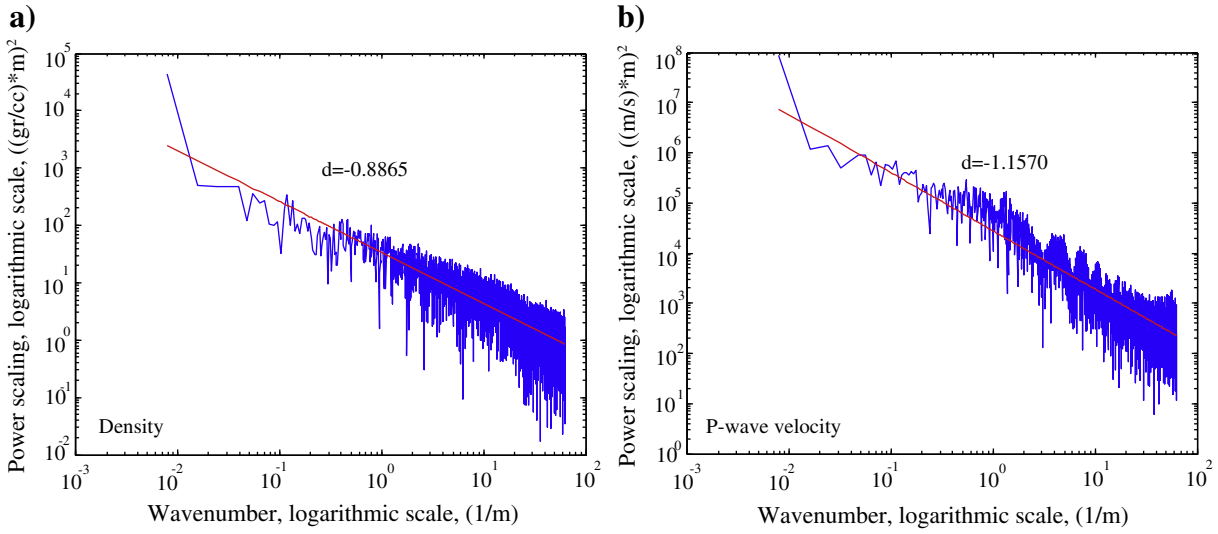

Fig. 4. 1D power spectrum of the density and Vp measurements from borehole B-353. Spikes from the data were filtered using a median filter before the calculation of the power spectrum. The red line represents a best least-square fitted line to the spectrum with a slope of "d". See text for discussion and interpretation of the results. (For interpretation of the references to color in this figure legend, the reader is referred to the web version of the article.)

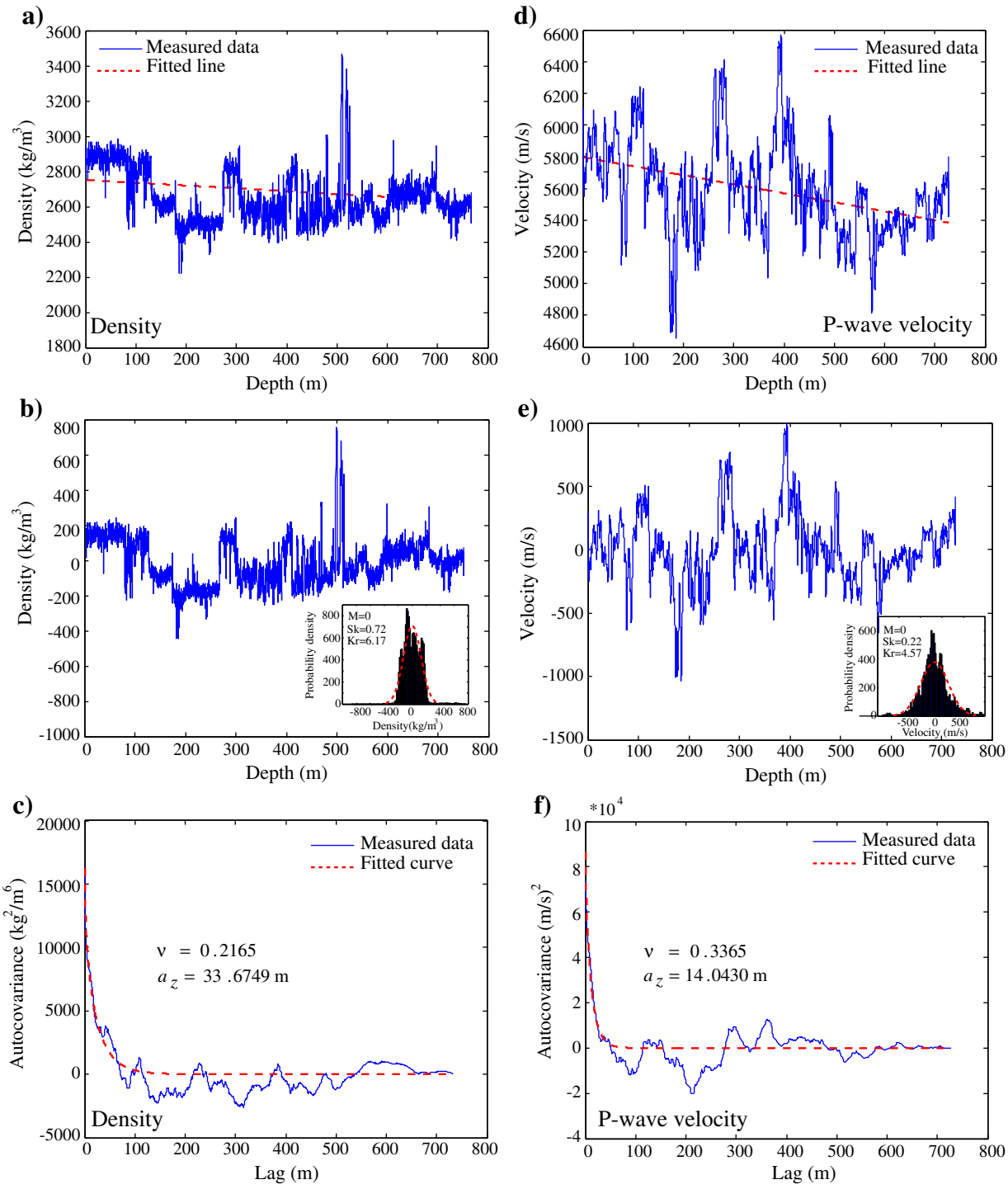

Fig. 5. Estimation of vertical scale length from the density and Vp logs of borehole B-353. (a) Measured density and best least-square linear fitted line to the data. (b) The stochastic part of density values after the removal of the general trend. The inset figure in (b) shows a Gaussian behavior of the stochastic part of the density data, which is a prerequisite for the estimation of scale length based on the von Karman method. The red dashed line shows a theoretical normal distribution, which is fitted to the probability density function of the stochastic part (M, Sk, and Kr are abbreviations for mean, skewness, and kurtosis, respectively). (c) Calculated autocovariance graph for the stochastic part of the density data shown in (b). The dashed curve in (c) represents the best-fitted 1D von Karman autocovariance function using a least-square method. (d) Measured Vp data and best least-square linear fitted line to the data. (e) The stochastic part of the Vp data after the removal of the general trend. The inset figure in (e) shows a Gaussian behavior of the stochastic part of the Vp data, which is a prerequisite for the estimation of scale length based on the von Karman method. The red dashed line shows a theoretical normal distribution, which is fitted to the probability density function of the stochastic part. (f) Calculated autocovariance graph for the stochastic part of the Vp data. The dashed curve in (f) shows the best-fitted 1D von Karman autocovariance function to the data. Vertical scale lengths are estimated to be 33 m and 14 m for the density and velocity data, respectively. (For interpretation of the references to color in this figure legend, the reader is referred to the web version of the article.)

which is not surprising given the short vertical scale length estimated from the logs. Due to lack of information, we assumed $a_x = a_z$ in this study. This assumption might not represent the complex geology in the area which clearly shows dominant westerly dips in the vicinity of boreholes B-357 and B-353. Horizontal correlation lengths could be longer along strike (N-S), but unfortunately, we have no means to constrain or confirm this hypothesis. Thus, the $a_x = a_z$ assumption likely represents an end-member scenario with possibly longer horizontal

Table 1
Estimated values of Hurst number (ν) and scale length for density, sonic Vp, and acoustic impedance log form borehole B-353.

Property	Hurst number	Scale length (m)
Density	0.2165	33.6749
Sonic Vp	0.3365	14.0430
Acoustic impedance	0.4986	19.5914

correlation lengths expected in reality. The consequences and limitations of this assumption on our results are addressed in the discussion.

5. Modeling of heterogeneity

We built several 2D models to investigate the scattering and seismic response in the presence of heterogeneity. Specifically, a detailed geological section in the Brunswick No. 6 area and circular and elliptical targets representing possible massive sulfide orebodies were considered for our models (Figs. 7 and 8; see Fig. 1 for location of the geological section). The geological section was constrained by surface geological observations, shallow and deep boreholes. The section extends down to more than 1 km depth (Fig. 7) and exhibits structural complexity of the subsurface formations in the Brunswick No. 6 area. In this model, the mineralized zones are represented by sheets embedded and deformed with the other lithological units.

By considering 2D von Karman autocovariance function (see Eq. (1)), we generated 2D heterogeneous models based on the scale length estimated from the acoustic impedance. Additional solutions considering different scale lengths for the velocity and density would complicate the seismic modeling results, and thus, were not considered. No shear-wave velocity (Vs) log is available from borehole B-353. Instead, shear-wave velocities were calculated assuming that they are about 55% of the Vp values. The generated 2D heterogeneous models (i.e., Vp, Vs and density with identical structure/realization) were gridded using 2 m by 2 m cell size. The length and depth of the models are 5 km and 2.5 km, respectively. Fig. 8a shows a 2D Vp model with an isotropic scale length of 20 m. In Fig. 8a, the target is a circular body with 62 m radius, centered in the model (x = 2500 m, z = 1250 m). Vp of the circular target is chosen to represent the massive sulfide layer (Brunswick horizon) intersected in borehole B-353. The density value used for the massive sulfide (4300 kg/m^3) is based upon sample measurements made in the Brunswick Mining Camp (Salisbury et al., 2003). Density

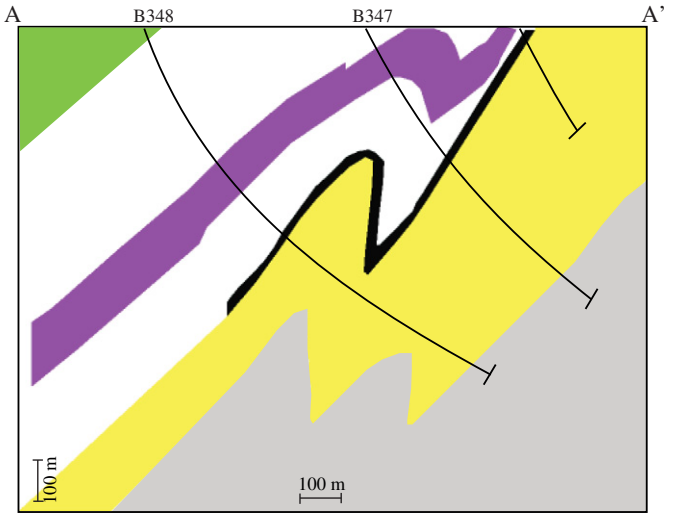

Fig. 7. Geological cross-section along the profile A–A′ shown in Fig. 1 obtained from a series of shallow and deep boreholes (B348 and B347) showing general structures of the Brunswick No. 6 area and associated Brunswick horizon (modified from Lentz and McCutcheon, 2006). The geological section combined with a heterogeneous medium is later used for the purpose of finite-difference seismic modeling. Legend for lithologies is the same as in Fig. 1. Note that there is no petrophysical data available from boreholes B348 and B347.

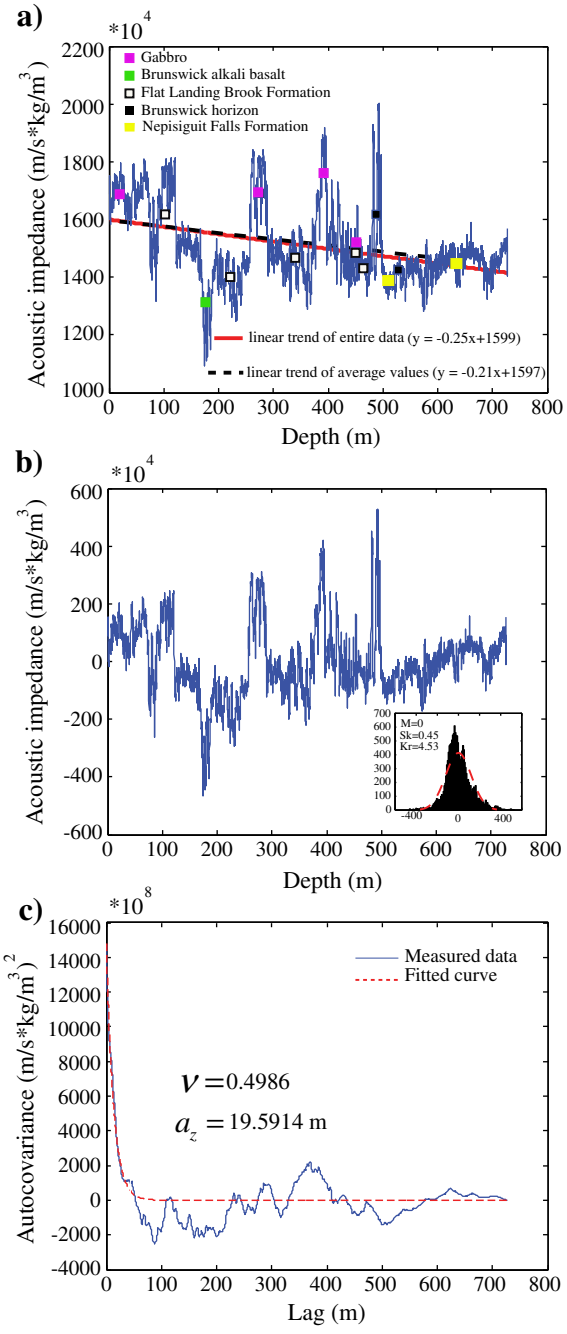

Fig. 6. Estimation of vertical scale length for the acoustic impedance (product of Vp and density) data from borehole B-353. (a) Calculated acoustic impedance and best linear least-square fitted lines for the entire data (solid line) and for average values within each individual geological formation (dashed line). Inset shows symbols used for each geological formation. Equations for both solid and dashed lines are also presented. (b) Stochastic part of the acoustic impedance data after the removal of the general trend (i.e., solid linear line). The inset figure in (b) shows the Gaussian behavior of the stochastic part of acoustic impedance data, which is a prerequisite for the estimation of scale length based on the von Karman method. The red dashed line shows a theoretical normal distribution, which is fitted to the probability density function of the stochastic part (M, Sk, and Kr are abbreviations for mean, skewness, and kurtosis, respectively). (c) Calculated autocovariance graph for the stochastic part of the acoustic impedance data shown in (b). The dashed curve in (c) represents the best-fitted 1D von Karman autocovariance function using a least-squares method. Vertical scale length is estimated to about 19.5 m (20 m is used in this paper) for the acoustic impedance data. (For interpretation of the references to color in this figure legend, the reader is referred to the web version of the article.)

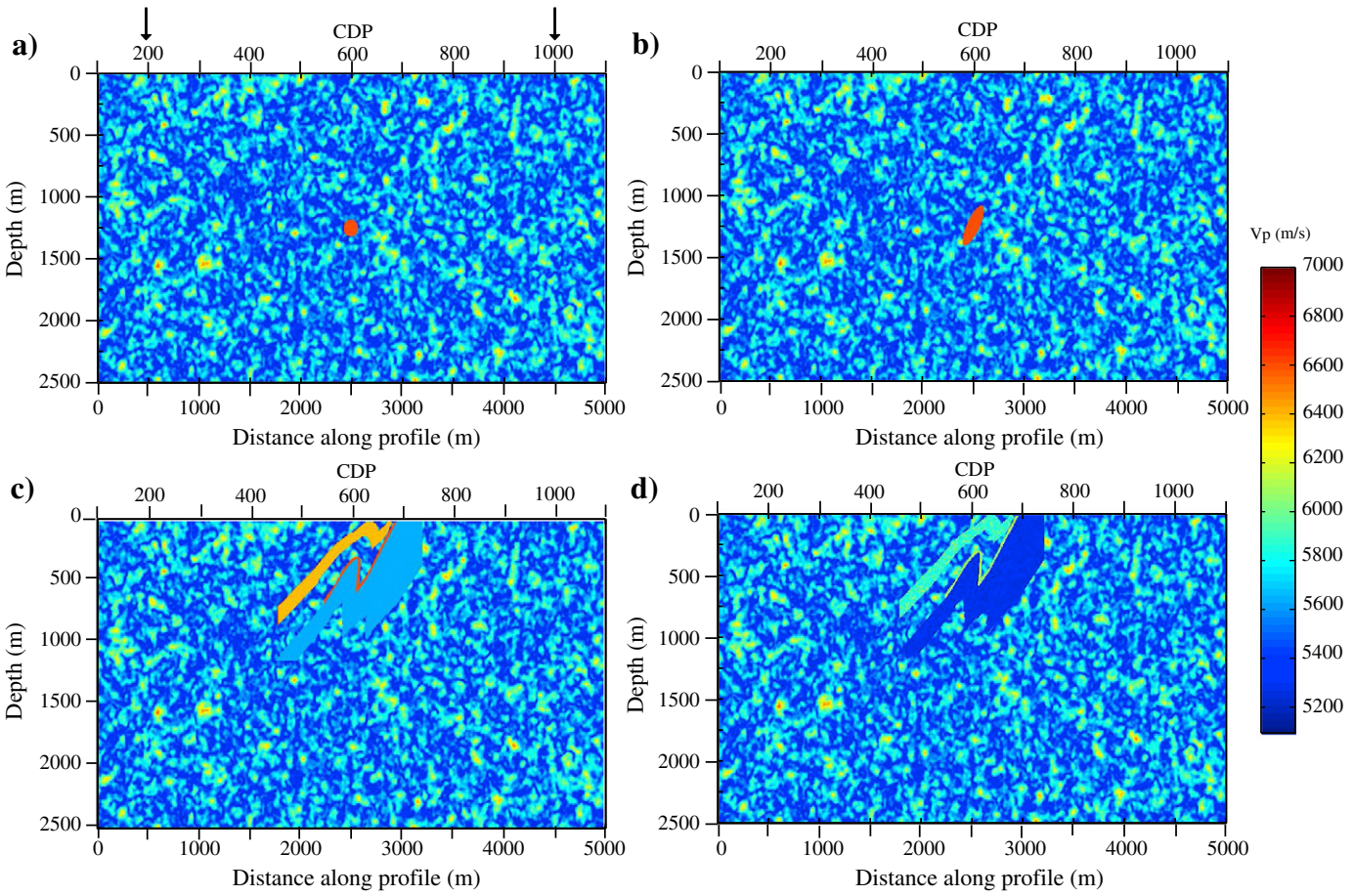

Fig. 8. Constructed Vp models for the medium based on an average vertical and horizontal scale length of 20 m and (a) circular target (massive sulfide), (b) elliptical target (massive sulfide), (c) geological section shown in Fig. 7, and (d) the geological section in Fig. 7, but with its own heterogeneity estimated from the log data within each individual geologic unit. The models were used to generate synthetic data using the elastic finite difference modeling method. The two arrows in (a) show the locations of the first and last synthetic shots generated over the models. CDP positions are also presented for all models.

measurements derived from gamma-gamma logging tools in the Brunswick No. 6 area saturate at approximately 3500 kg/m^3, and as a result, do not provide realistic density measurements of massive sulfide ore (Malehmir et al., 2013; Mwenifumbo et al., 2005). A spherical body (3D) with an equivalent 2D cross-section could then host about 4 Mt (density 4300 kg/m^3) massive sulfide minerals, and could represent an economic deposit. Fig. 8b shows a 2D heterogeneous model with an elliptical target located at the center of the model. The minor axis of the ellipse is equal to the radius of the circular target in Fig. 8a and the major axis is 2.5 times the minor axis. The ellipsoidal body is tilted 60° to the west, following the general dip direction of the geological formations in the study area. Properties of the elliptical target are the same as the circular target in Fig. 8a. Such a lenticular body in 3D could contain about 6 Mt of massive sulfide minerals. In Fig. 8c, the geological cross-section shown in Fig. 7 is superimposed on the heterogeneous background model and used as a target for the elastic FD modeling. Physical rock properties observed in the logging data were assigned to the lithological units shown in the cross-section. Values of Vp and density for gabbro, the massive sulfide formation (or Brunswick horizon), and the Nepisiguit Falls Formation are shown in Table 2. Fig. 8d shows the same geological section as shown in Fig. 8c, except that the heterogeneity within each formation is also included separately and accounted for in the seismic modeling.

6. Elastic finite difference modeling of heterogeneous medium

Synthetic seismic data were generated using an elastic FD algorithm (Juhlin, 1995), with identical parameters and acquisition geometry for all the models shown in Fig. 8. A free surface condition at zero depth and absorbing boundaries were used for the modeling. We simulated 500 receiver positions (vertical geophone) placed every 10 m along the entire length of each model, and 100 synthetic shots placed at every 40 m over a 4 km section of each model (see two arrows in Fig. 8a). The simulated shots are at 4 m depth. An explosive Ricker wavelet source with a center-frequency of 70 Hz and a 2 ms sampling rate were used to generate the synthetic seismograms (actual time stepping in the FD modeling was 0.000181 s).

The synthetic seismic data were processed using a prestack DMO and poststack migration strategy (Table 3) similar to that used by Cheraghi et al. (2011) to process the real 2D profiles. The CDP positions for each model are shown in Fig. 8. Figs. 9 and 10 show example synthetic shot gathers from the models. For comparison, a real shot gather along the BRN991001 2D profile is also presented in Fig. 10 (see Fig. 1 for location of the shot). All synthetic shot gathers in Figs. 9 and 10 are located at 2360 m (horizontal distance) along the model. Raw shot gathers (Figs. 9 and 10) show strong direct compressional- and shear-waves (direct shear-wave is muted for

Table 2
Average compressional-wave velocity (Vp) and density of various geological formations in the Brunswick No. 6 area obtained from borehole B-353 (see Fig. 2).

Lithology	Vp (m/s)	Density (kg/m^3)
Gabbro	6400	3000
Massive sulfide	6600	4300
Nepisiguit Falls Formation	5650	2700

Table 3
Processing sequence used to process the synthetic seismic data for all the models shown in this study.

Step	Parameters
1.	Read 1.0 s SEGY data
2.	Geometry set-up
3,.	Direct P-wave arrival attenuation
4.	Direct S-wave arrival attenuation (near-offset)
5.	Median filtering
6.	Velocity analysis (iterative)
7.	NMO corrections
8.	DMO corrections
9.	F-K filtering
10.	Stack
11.	Migration (Stolt)

presentation purposes), and back-scattered shear-waves, which are generated by strong near-surface heterogeneities.

Fig. 9a shows a shot gather from the model shown in Fig. 8a (i.e., the circular target). Diffractions (top and bottom) from the circular target are observable (Fig. 9a). Fig. 9b shows a shot gather over the elliptical target. Direct compressional- and shear-waves as well as the scattered shear-wave (hatch-shape) can be seen on the raw shot gather. A diffraction from the elliptical target can also be distinguished on the shot gather.

Fig. 10a, b shows the shot gathers from the models shown in Fig. 8c, d. Reflections from the gabbroic unit (Gb) and massive sulfide formation (Msl; Brunswick horizon) are observed on the shot gathers. The simulated shot gathers show some similarities with the field shot gather. For example, direct compressional- and shear-waves have relatively similar velocities in both the synthetic and real shots, implying that the average velocities estimated for the medium are realistic. The gabbro unit is observable in both the synthetic and the real shots (Fig. 10). One of the main differences between the synthetic and real shots is the strong back-scattered shear-waves (Fig. 10) observed in the synthetic data. Although this might indicate that the stochastic component of the models is unlikely, there are other reasons that can explain this difference. For example, the presence of relatively thick unconsolidated sediments (overburden) in the study area is not taken into account in our modeling. In our models, shear-waves propagating horizontally at the surface will intersect the heterogeneity (models in Fig. 8a, b) and/or lithological contacts (models in Fig. 8c, d) producing the back-scattered energy observed on the synthetic gathers. In the field, shear-waves propagating at the surface will travel mostly in the overburden. In addition, the amplitudes of the shear-waves in the simulated

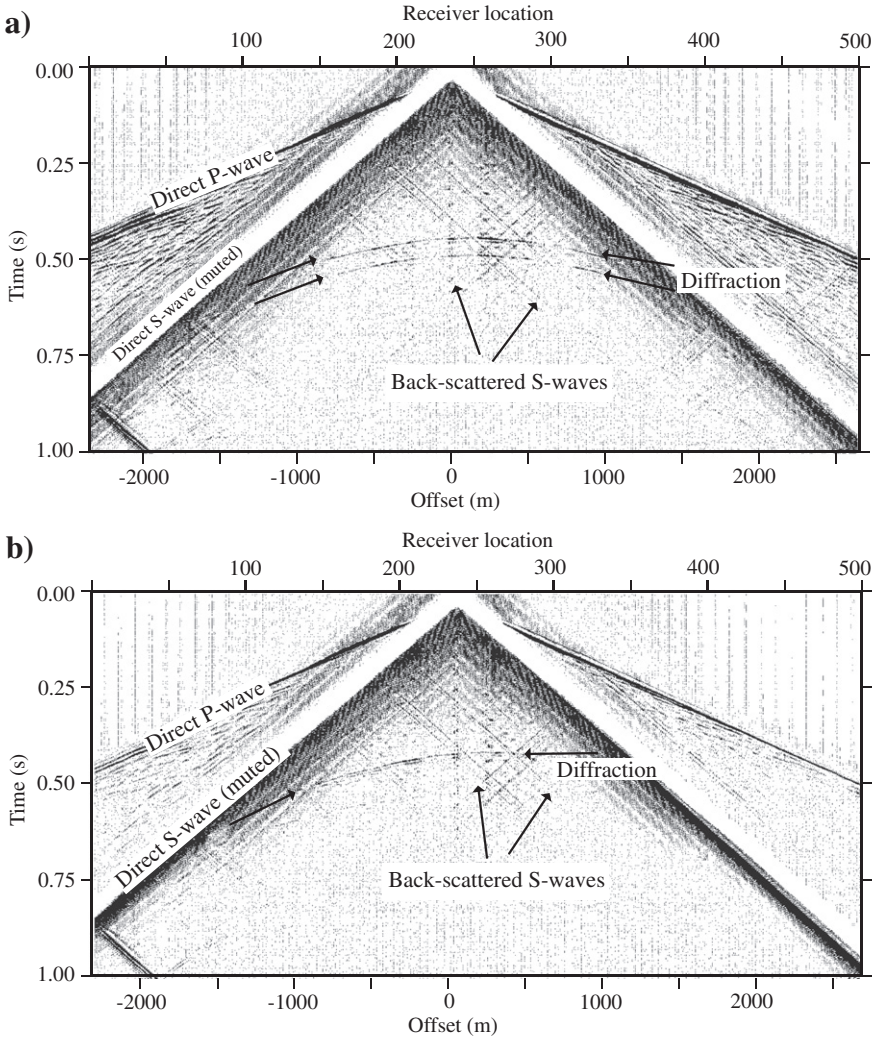

Fig. 9. (a) Raw synthetic shot gather (vertical component) from the model with a circular target (Fig. 8a) at x = 2360 m along the model. Symmetric hyperbolic-shaped diffracted waves (top and bottom) from the circular target and back-scattered shear-waves from the near-surface heterogeneities are present. (b) Raw synthetic shot gather (vertical component) from the model with the elliptical target (Fig. 8b) at x = 2360 m along the model. Asymmetric hyperbolic-shaped diffracted waves from the elliptical target and back-scattered shear-waves are present. In comparison with the circular target, the elliptical target generates only one diffraction. The direct shear-wave is muted in (a) and (b) only for display purposes, due to their high-amplitude energy. See text for details.

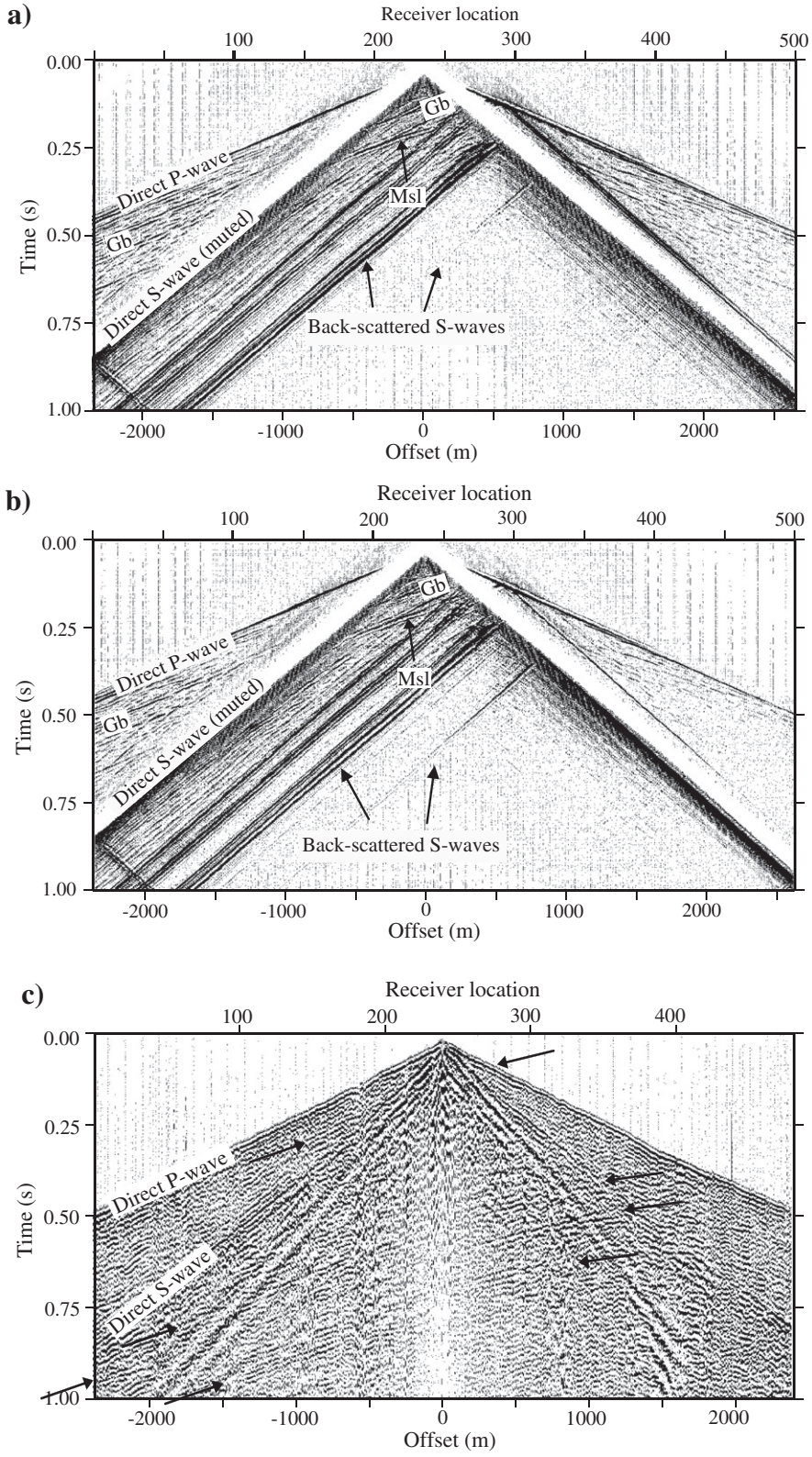

Fig. 10. (a) Raw synthetic shot gather (vertical component) from the model with the geological section shown in Fig. 8c. Gb and Msl are signals from the gabbro and massive sulfide formation (see Fig. 7). (b) Raw synthetic shot gather (vertical component) from the model shown in Fig. 8d. Direct shear-wave is muted in (a) and (b) for display purposes. (c) A raw shot gather from the BRN991001 2D profile shown in Fig. 1; the arrows indicate the observed reflections in the shot gather. See text for details.

gathers appear slightly overestimated when compared to the real data, also explaining why the back-scattered shear-waves appear so strong on the synthetic gathers. Furthermore, no attenuation was introduced into the models. A highly attenuating near-surface would significantly reduce the amplitudes of the back-scattered direct waves. These are all examples of the limitations with the modeling carried out in this study and should be taken into account before any conclusion is drawn. An additional complication to all these is the absence of shear-velocity information from the study. The back-scattered shear-waves were damped from the synthetic shot gathers using median

and F-K filters (Table 3). Fig. 10c also shows long and high amplitude reflections (see arrows in Fig. 10c) that are clear in the shot gather between 0.5–1 s. These reflections originate from deeper structures that were not considered or introduced into the model.

7. Results

Figs. 11 and 12 show DMO-corrected unmigrated stacked and migrated stacked sections of all models. Fig. 11a and b shows a portion of the stacked and migrated sections of the circular target (see Fig. 8a), respectively. The symmetric (in terms of shape and amplitude) hyperbolic response of the top and base of the circular target is observed in Fig. 11a. Fig. 11b shows how the diffractions collapse (top and base) into a local semi-circular shape. Weak scattered signals from the heterogeneous medium are also observed in Fig. 11a, b. Fig. 11c and d shows a portion of the stacked and migrated sections of the elliptical target (see Fig. 8b) down to 0.75 s. The diffractions (Fig. 11c) are asymmetric, both in terms of their shape and amplitudes. Scattered signals due to the heterogeneous medium are also evident in both sections (Fig. 11c, d).

Fig. 12 shows the DMO-corrected unmigrated stacked and migrated stacked sections of the models shown in Fig. 8c, d. Gb and MSI are reflections from the gabbro and massive sulfide formation, respectively (see Figs. 7 and 10). Since the geometry and processing procedure for both models shown in Fig. 8c, d are similar, it is possible to analyze the effect of heterogeneity within each individual geological unit. Comparison of the results suggests that reflections are similar in both models, but are slightly weaker where internal heterogeneity has been introduced (e.g., see Msl in Fig. 12a and c). In order to better understand the effects of heterogeneity in imaging mineral deposits, we generated a model with geometry and physical properties of the model shown in Fig. 8b (ellipse) but embedded in a homogeneous background with Vp, Vs, and density of 5650 m/s, 2850 m/s, and 2700 kg/m^3, respectively. These values are equal to the mean values of the observed measurements from borehole B-353 (Fig. 2). Fig. 13 shows the DMO-corrected unmigrated stacked and migrated stacked sections from this model. In comparison with Fig. 11c and d, diffractions of the elliptical target and the resultant migrated image in the homogeneous case are clearer. Scattered signals from the heterogeneous medium obscure the seismic response from the target, especially in the migrated section. Amplitude directivity for the diffractions in the down dip direction is evident in both Figs. 11 and 13.

8. Discussion

Comparisons between the migrated seismic sections obtained in the homogeneous and heterogeneous mediums (see Figs. 11 and 13) suggest that seismic scattering effects in the heterogeneous medium complicate the identification of the bright-spot anomaly associated with the massive sulfide targets. Diffractions from massive sulfide targets remain identifiable in the DMO-corrected unmigrated stacked sections (Fig. 11), but are partly masked by small-scale scattering,

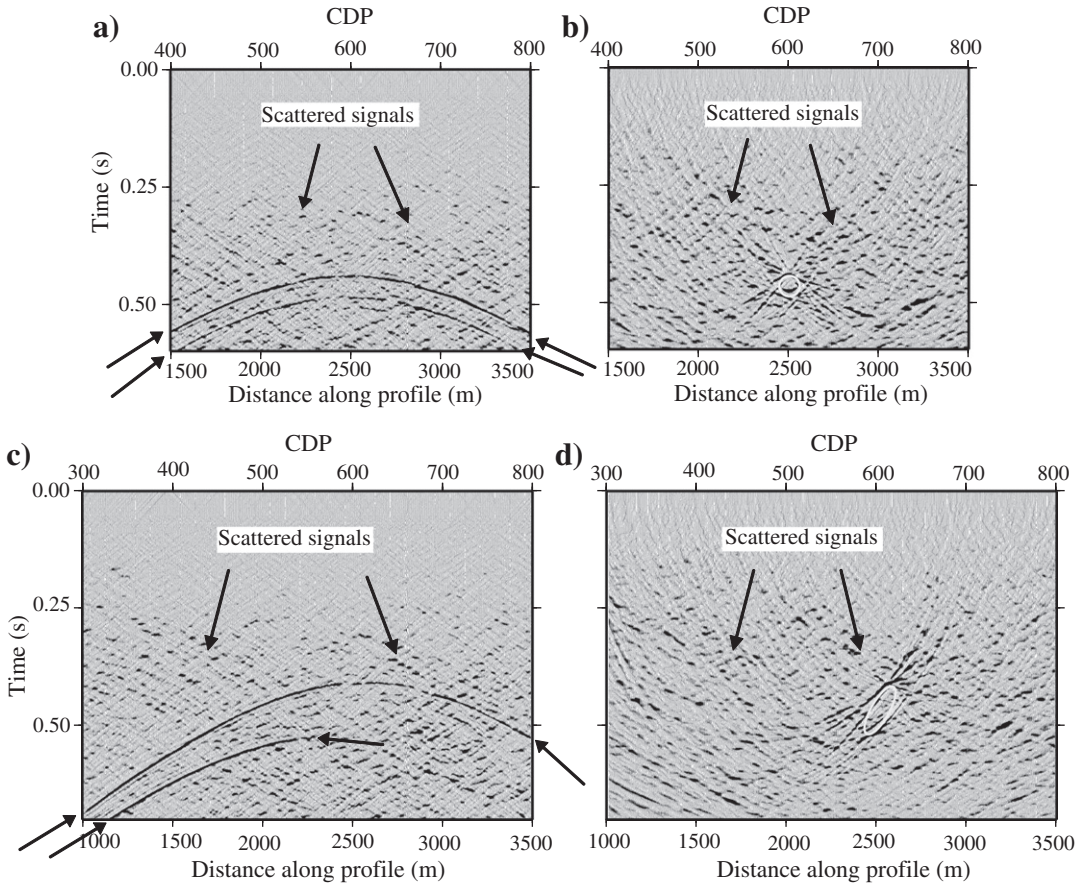

Fig. 11. (a) DMO-corrected unmigrated stacked section between CDPs 400 and 800 over the model shown in Fig. 8a. The arrows on (a) mark diffractions generated from the top and the base of the circular target. Scattered signals from the heterogeneous medium are also visible. (b) Migrated stacked section of (a); white circle represents the spatial position of the circular target. Strong scattered signals from the heterogeneous medium are also visible. Note that the seismic signal, although observable in the migrated section, can be missed by an interpreter's eyes. (c) DMO-corrected unmigrated stacked section between CDPs 300 and 800 over the model shown in Fig. 8b. The arrows on (c) mark diffractions generated from the top and the base of the elliptical target. Scattered signals from the heterogeneous medium are also visible. (d) Migrated section of (c); white ellipse represents the spatial position of the elliptical target. The asymmetric diffractions (in terms of amplitude variations along the diffraction) are collapsed into the location of the elliptical target. Scattering signals from the heterogeneous medium are also visible. This seismic signal is also observable in the migrated section but could be mis-interpreted as a short reflection.

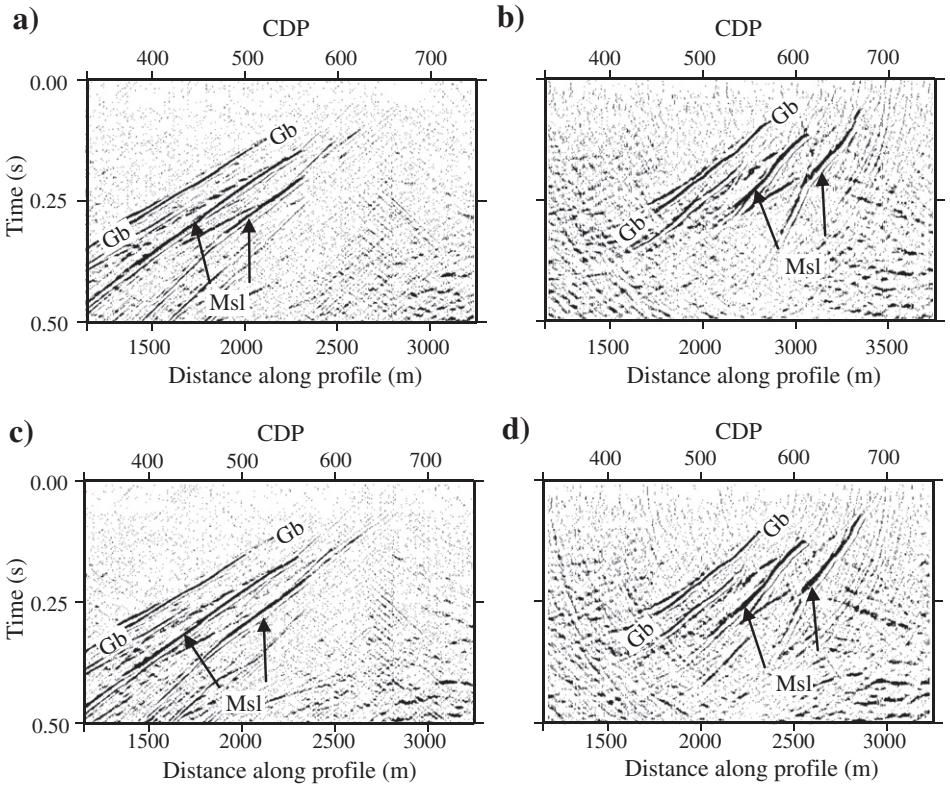

Fig. 12. (a) DMO-corrected unmigrated stacked section over the geologic cross-section (with no internal heterogeneity) and model shown in Fig. 8c between CDPs 330 and 750. See text for interpretation of Gb and Msl reflections. (b) Migrated section of (a) which shows the difficulty of surface seismic methods in imaging the steeply dipping structures of the Brunswick No. 6 area. (c) DMO-corrected unmigrated stacked section over the geologic cross-section (with internal heterogeneity) and the model shown in Fig. 8d between CDPs 330 and 750. See text for interpretation of Gb and Msl reflections. (d) Migrated section of (c).

particularly where the amplitude of the diffraction is weaker, in the seismograms of the heterogeneous models. These results are based on a series of estimated parameters and assumptions, some of which may not provide an accurate representation of the geological environment near the Brunswick No. 6 deposit. In this section, we present results obtained using different parameters to assess how the choice of certain parameters influences the results and to provide some constraints on what parameters are realistic for this area. In particular, the effects of different horizontal and vertical scale lengths, source frequency, and heterogeneity fluctuations are evaluated and discussed.

8.1. Effects of horizontal and vertical scale lengths

8.1.1 . Longer horizontal scale lengths

As mentioned previously, the cross-correlation of the two boreholes did not allow estimating the horizontal scale length (a_x). We generated three additional models to evaluate the impact of the

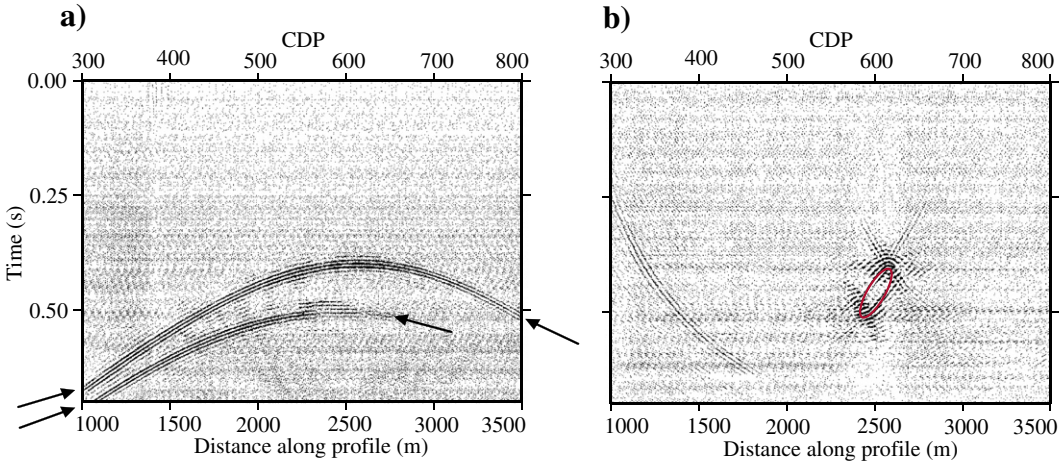

Fig. 13. (a) DMO-corrected unmigrated stacked section between CDPs 300 and 800 over a homogeneous medium and an elliptical target with a geometry similar to the model shown in Fig. 8a. The arrows show asymmetric diffractions from the top and base of the elliptical target. (b) Migrated section of (a); red ellipse represents the spatial position of the target. In comparison with the model with the heterogeneity, the homogeneous model clearly shows a complete diffraction signal with clear flanks at least from the top of the target embedded in the homogeneous medium. (For interpretation of the references to color in this figure legend, the reader is referred to the web version of the article.)

$a_x = a_z$ assumption used in our study. These models (Fig. 14) have horizontal scale lengths on the order of the seismic wavelength (i.e., 1λ, 2λ, and 20λ). For a given wavelength of 70 m (i.e., wavelength in the dip direction) and scale length of 20 m normal to the dip direction, we will have a_x/a_z that are 4, 7, and 70, respectively. These three aspect ratios were used when generating Vp, Vs, and density models of the medium. We also rotated the main axis of the scale length such that the horizontal scale length now follows the direction of the geological dips (~60º) in the area. An elliptical body with the properties and dimension of the massive sulfide shown in Fig. 8b was used as the target. The main motivation here was to investigate the effects of longer horizontal length, when conventional post-stack migration processing algorithms based on the assumption of isotropy are used.

The DMO-corrected unmigrated stacked and migrated stacked sections of the three different models are also shown in Fig. 14. Note that a new velocity analysis was performed separately for each simulated seismic data set shown in Fig. 14 to account for the complexity introduced in the new models. However, no anisotropy parameters were considered in the seismic modeling and processing although the models are now fairly anisotropic. A thorough evaluation of the effect of anisotropy will be investigated in future work. However, it is clear that the heterogeneity in the direction of wave propagation and perpendicular to the direction of propagation can have quite different effects on the coherence of the propagating wave front. The stacked sections in Fig. 14d–f clearly show that the diffractions from the elliptical target are preserved and observable for the corresponding models. However, the migrated seismic sections show a distorted collapse of the diffractions (Fig. 14h–i), making the identification of the target more difficult than in the example previously presented in Fig. 11d. This implies that high amplitude seismic signals from small but yet economically feasible massive sulfide deposits may be masked by the strong heterogeneity in a strongly deformed and metamorphosed medium. These results are in agreement with L'Heureux et al. (2009) who concluded that for scale lengths similar or longer than the seismic wavelength, scattering produces highly reflective (noisy) seismic signals that can dominate seismic records and complicate the identification of the response of smaller targets.

However, it is important to reiterate that diffractions are still readily observed on the DMO-corrected stacked sections for any of the horizontal scale lengths tested in this paper, but that the delineation of the target would not be possible using conventional processing methods. The

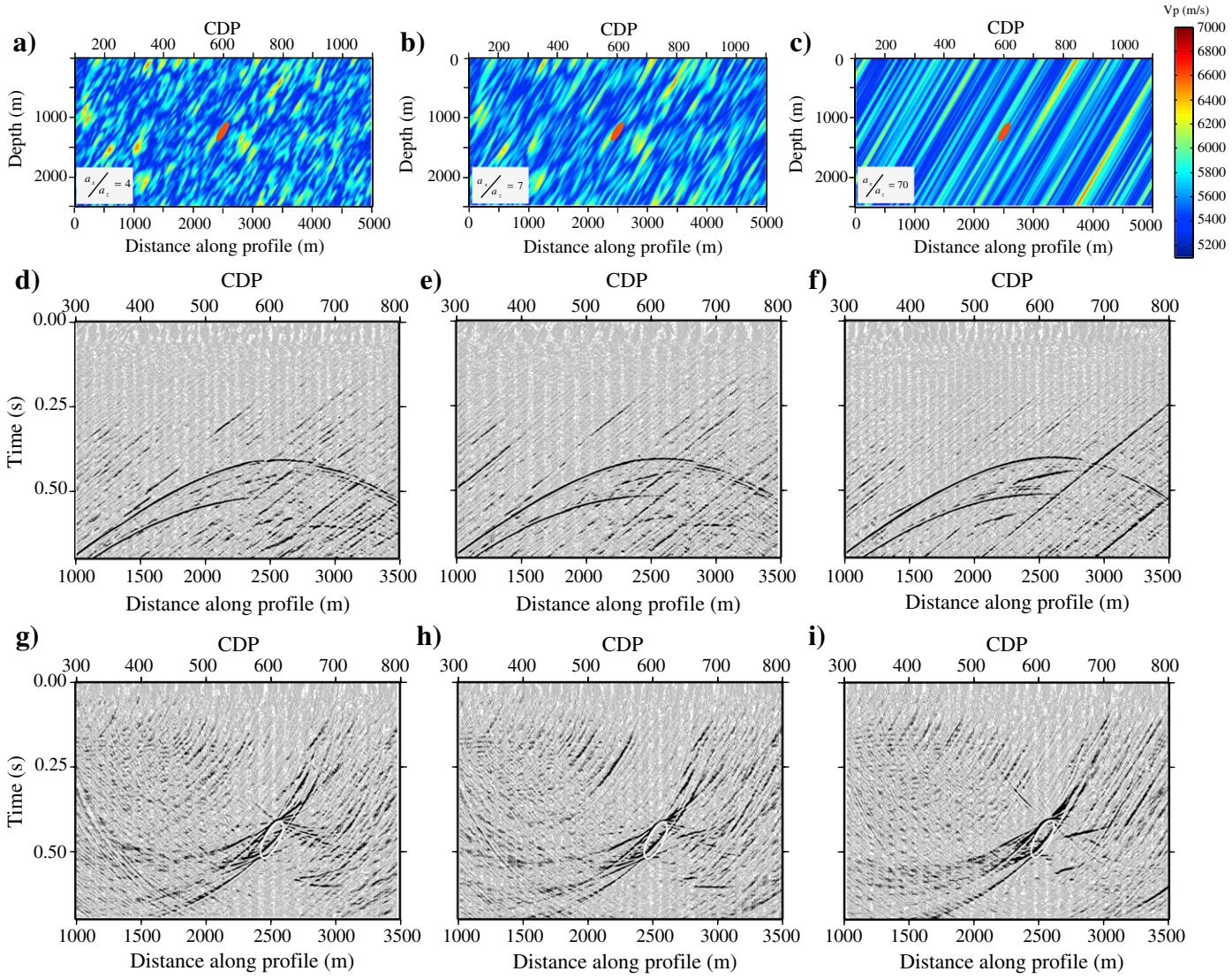

Fig. 14. Constructed Vp models for the elliptical target (massive sulfide) shown in Fig. 8b with aspect ratios (a) $a_x/a_z = 4$, (b) $a_x/a_z = 7$, (c) $a_x/a_z = 70$. (d, e, and f) DMO-corrected unmigrated stacked sections of the models shown in (a, b, and c). (g, h, and i) Migrated stacked sections of models shown in (a, b, and c). Note that the elliptical target produces diffractions in the stacked sections that are clearly identifiable. On the other hand, the seismic signal in the migrated seismic sections is partly masked by the heterogeneity introduced in the models. Slight mis-locations of the target are also clear in the migrated seismic sections.

migrated seismic sections show (Fig. 14h–i) slight mis-locations of the target due to the structural anisotropy introduced by the longer horizontal scale lengths, further supporting the conclusions of anisotropy on travel path and length as previously discussed by Bongajum et al. (2012).

8.1.2. Shorter vertical scale lengths

The calculated scale length from the acoustic impedance log (a_z = 20 m; see Fig. 6) represents the maximum scale length at which the medium scales with a power law. While the maximum scale length is used in the modeling, it may not entirely characterize the stochastic environment in the Brunswick No. 6 area (see also Goff and Holliger, 1999). We further investigated the impact of smaller scale-lengths (see also Flatté et al., 1979; Holliger, 1997; Wu and Aki, 1988) by re-analyzing the model shown in Fig. 8b with a scale length less than 20 m. A new model representing $a_x = a_z = 10$ m was generated while the remaining realization parameters were kept similar to that used to generate the model shown in Fig. 8b. To make the comparison easier, the two models are shown in Fig. 15.

In the models shown in Fig. 15, the smaller scale length (10 m, Fig. 15a) produces weaker diffractions from the target (Fig. 15c). The migrated stacked sections (Fig. 15e, f) exhibit similar characteristics to the DMO-corrected unmigrated stacked sections (Fig. 15c, d). This analysis reveals that scale lengths less than the estimated value from the autocovariance function (i.e., the maximum scale length) weakens the diffractions signal from the target. These results are surprising since as the scale length becomes smaller, one would expect that the medium would tend to become more homogeneous (Wu and Aki, 1988). However, we observe exactly the opposite. Based on the parameters used (i.e., scale length, wavelength, and travel path length) and according to Wu and Aki (1988), the models tested (we also tested a 15 m scale length, but not shown here) in this study fall within a weak-scattering regime. Therefore, a sudden change in the scattering regime is not expected from a 20 m to 10 m scale

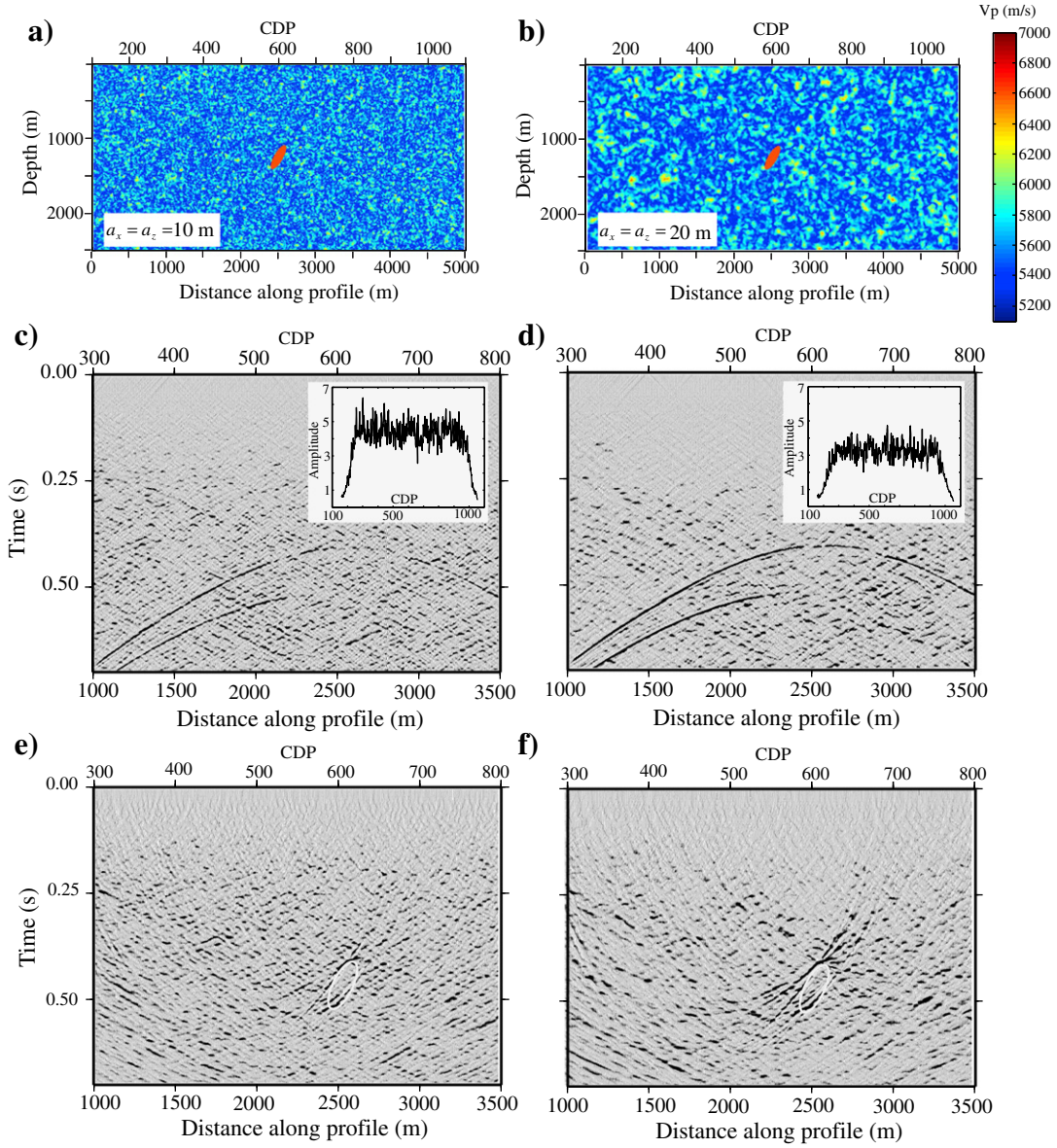

Fig. 15. Constructed Vp models for the elliptical target (massive sulfide) shown in Fig. 8b with scale lengths (a) $a_x = a_z = 10$ m and (b) $a_x = a_z = 20$ m. (c and d) DMO-corrected unmigrated stacked sections of the models shown in (a and b). (e and f) Migrated stacked sections of the models shown in (a and b). Note that the elliptical target produces weaker diffractions for the model with smaller scale length. The model shown in (a) generates very strong scattering as illustrated by the RMS amplitudes calculated for a window between 0 ms to 320 ms (see inset figures on (c) and (d)). See text for detailed discussion about the modeling results.

length. In order to better understand the results, we calculated the RMS amplitudes of the unmigrated stacked sections above the target (between 0 ms to 320 ms) for the models (see inset figures shown in Fig. 15). The 10 m scale length model generates higher scattering amplitudes in comparison with the 20 m scale length model. This can be explained by a larger number of small scatterers with stronger acoustic impedances for the model with the 10 m scale length. This is because the generated models follow a Gaussian distribution (an assumption made for the generation of the models and the media), implying that the mean and standard deviation are kept fixed for the 10 m and 20 m models. As a result, a larger number of scatterers with larger contrast with the target are generated to maintain this distribution when smaller scale lengths are used in the models (Fig. 15). This implies that the observed scattering for the smaller scale length is overestimated. Future studies aiming to investigate the effect of scale length should preserve the relative strength of the heterogeneity versus background (for different scale lengths). Nevertheless, it is worthwhile mentioning that the scattering from heterogeneity in the two models presented here does not entirely mask the target response on the DMO-corrected stacked sections, a point that is the main focus of our study.

8.2. Effects of source frequency

To investigate the effects of the frequency on seismic imaging of mineral deposits within heterogeneous environment, we also generated synthetic shots using 50 Hz and 90 Hz source center-frequencies for the model presented in Fig. 8b (lenticular target). Fig. 16 exhibits DMO-corrected unmigrated stacked and migrated stacked sections for these scenarios. As expected, the scattering from the medium decreases with the increasing source frequency. It is interesting to note that the diffraction signal from the target becomes more coherent and stronger with a source frequency of 90 Hz (Fig. 16c). This implies that higher frequency seismic sources can be very helpful not only for improving seismic resolution but also to preserve diffractions in heterogeneous media with small scale lengths.

8.3. Effect of heterogeneity fluctuations

To investigate if an increase in the fluctuations of acoustic impedance could move the media from a weak to a strong scattering regime we again considered the model shown in Fig. 8b but varied the fluctuations from one standard deviation (σ_{lm}) to one and a half standard deviation ($1.5\sigma_{lm}$). Higher fluctuations (e.g., $2\sigma_{lm}$ or $3\sigma_{lm}$) were not considered because they generate velocities above 7000 m/s, which are very unlikely in this geological environment. To make the comparison easier, results for one standard deviation (σ_{lm}) and one and a half ($1.5\sigma_{lm}$) are shown in Fig. 17. Fig. 17b ($1.5\sigma_{lm}$) shows scatterers with higher velocities in the medium, which introduce strong scattering in both the unmigrated stacked and migrated sections (c.f., Fig. 17d and f v.s. Fig. 17c and e). Also, the signal from the target (Fig. 17d and f) is much weaker relative to the background signal when larger fluctuations are introduced. The stronger parts of the diffractions are still observable in the DMO-corrected stacked section; however, the target is very weak in the migrated section.

While scattering and stochastic modeling in the crystalline environment can be further studied and debated, this study demonstrates that even in unfavorable conditions (e.g., variable scale length, low-to-moderate seismic source frequency, large velocity or heterogeneity perturbations), imaging of economical sized mineral deposits in

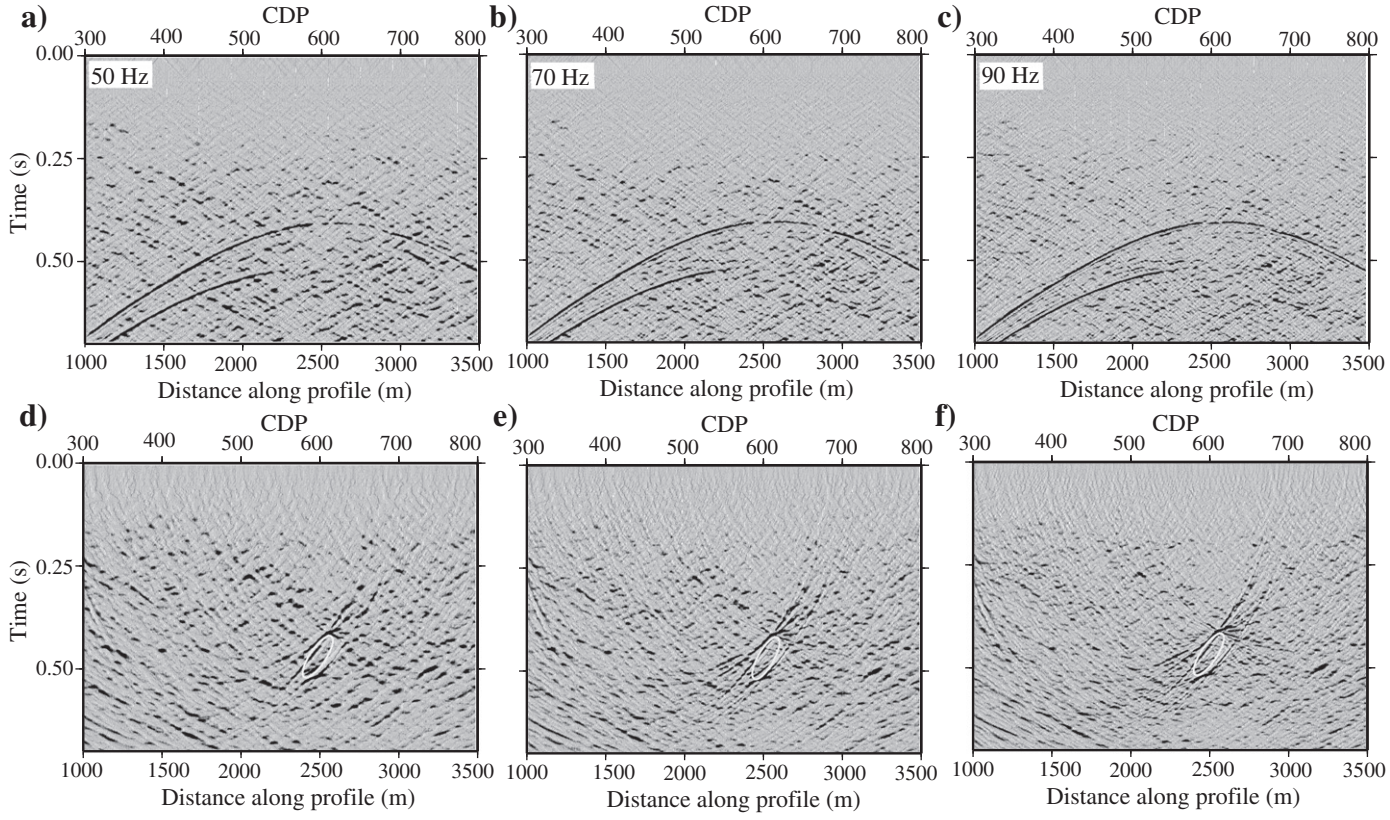

Fig. 16. (a, b, and c) DMO-corrected unmigrated stacked sections of the models shown in Fig. 8b with central source frequency of 50 Hz, 70 Hz and 90 Hz. (d, e, and f) Migrated stacked sections of (a, b, and c). Note that the elliptical target shows the weakest diffraction signal in the stacked section for 50 Hz central source frequency shown in (a). Also, the scattering from the medium is strongest in (a) and (d). The highest frequency (90 Hz) shows the strongest diffraction signal (c) from the target and the weakest scattering from the medium.

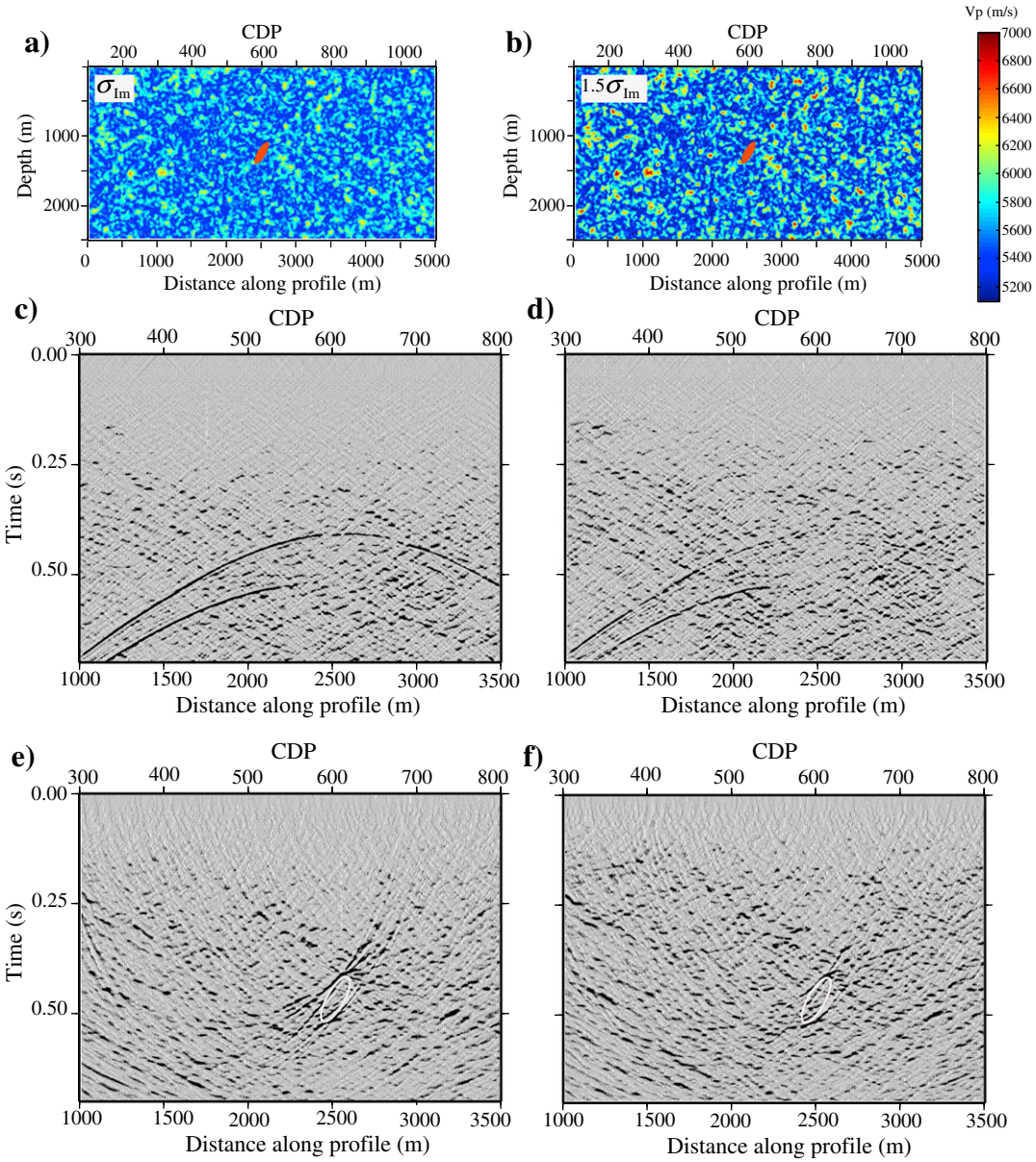

Fig. 17. Constructed Vp models for the elliptical target (massive sulfide) shown in Fig. 8b but with increasing fluctuations in the acoustic impedance. (a) Equal to one standard deviation (σ_{Im}), and (b) equal to one and a half standard deviation (1.5 σ_{Im}). Note that these Vp models are generated from the scale length estimated from the acoustic impedance. (c and d) DMO-corrected unmigrated stacked sections of the models shown in (a and b). (e and f) Migrated stacked sections of the models shown in (a and b). Note that by increasing fluctuations in the heterogeneous medium the diffraction signal from the target becomes difficult to distinguish both in the unmigrated stacked and migrated sections.

the Brunswick No. 6 mining area is possible. The clearest signature from massive sulfides is on the DMO-corrected stacked sections. However, in the presence of heterogeneity, both flanks of the diffractions are often disturbed for a dipping lenticular orebody (Figs. 8 and 11). The flank in the dip direction will have stronger amplitude compared to the opposite flank which will have considerably weaker amplitudes. Therefore, poor or conventional processing may not be able to properly image the diffraction, and an image that appears more as a reflection than a diffraction may be produced (see Eaton, 1999; Malehmir and Juhlin, 2010). This suggests that new processing strategies should be considered to attenuate the effects of the heterogeneous medium and obtain better post-stack migrated images. For example, a processing approach focused on diffractions in the unmigrated stacked sections or prestack data might be worthwhile to improve the detection of massive sulfide deposits (see Berkovitch et al., 2009; Dell and Gajewski, 2011; Khaidukov et al., 2004). Our results demonstrate that an efficient processing approach for mineral exploration should address both the low signal-to-noise ratio often observed in the crystalline environment and the effects of heterogeneity, although the two are sometimes related.

9. Conclusions

Scaling behavior or cyclicity of geological formations over the Brunswick No. 6 area was investigated using available borehole petrophysical logs. The borehole petrophysical measurements allowed the estimation of the vertical scale length by statistical methods. The estimated vertical scale length is around 20 m (from acoustic impedance) in the study area. However, our seismic modeling studies based on this scale length assumption demonstrate that in even this theoretically weak scattering regime effective imaging of small geological targets such as massive sulfide deposits, especially in the migrated stacked sections can be challenging. Diffraction signals from the massive sulfide deposits are visually easier to identify in the unmigrated stacked sections, implying

that analyses should focus on the unmigrated stacked sections and prestack data rather than the migrated stacked sections. Testing heterogeneous models with different scatterer aspect ratios and horizontal scale lengths much larger than the vertical scale length showed that the heterogeneous medium not only could generate coherent noise in the form of high amplitude signals that mask the imaging of ore bodies, but also results in slight mis-location of the target if isotropic processing methods are used. Testing seismic response of a lenticular target with frequency range of 50–90 Hz indicates that lower frequencies introduce more scattering into the seismic image and could mask the target response. We also observed that higher source frequencies lead to stronger diffraction signal from the target. Also, comparisons of models with different standard deviations for the acoustic impedance fluctuations showed that increasing standard deviation causes more scattering in the model to a point that even observing the diffraction signal from the target can be difficult. The seismic image from the model with a smaller scale length than the maximum fractal dimension (20 m) showed stronger scattering and a weaker diffraction signal. However, further tests are required to verify if such a result may be expected in the real world. Our analyses demonstrate the value of detailed geophysical studies and borehole petrophysical measurements, which can be helpful to better understand the seismic response from the medium and any geologic target within it.

Acknowledgments

The authors thank Xstrata Zinc for providing access to the petrophysical and seismic data in the Brunswick No. 6 area. Saeid Cheraghi wishes to thank the Iranian Academic Center for Education, Culture and Research (ACECR), Isfahan University of Technology Branch for funding his research PhD position. This work is a joint collaboration between Uppsala University and the Geological Survey of Canada. GLOBE Claritas™ was used for the synthetic seismic data processing. GMT from P. Wessel and W.H.F. Smith was used to prepare some of the figures. We are thankful to F. Zhang and C. Juhlin for their technical help during the model preparation and seismic modeling. We acknowledge the critical reviews by two anonymous reviewers along with those provided by the editor, which helped improve the quality of our paper. Geological Survey of Canada contribution 20120174.

References

Adam, E., Perron, G., Milkereit, B., Wu, J., Calvert, A.J., Salisbury, M., Verpaelst, P., Dion, D.J., 2000. A review of high-resolution seismic profiling across the Sudbury, Selbaie, Noranda, and Matagami mining camps. Canadian Journal of Earth Sciences 37, 503–516.

Adam, E., Perron, G., Arnold, G., Matthews, L., Milkeriet, B., 2003. 3D seismic imaging for VMS deposit exploration, Matagami, Quebec. In: Eaton, D.W., Milkereit, B., Salisbury, M.H. (Eds.), Hardrock Seismic Exploration. Society of Exploration Geophysicists, pp. 229–246.

Bansal, A.R., Gabriel, G., Dimri, V.P., 2010. Power law distribution of susceptibility and density and its relation to seismic properties: an example from the German Continental Deep Drilling program (KTB). Journal of Applied Geophysics 72, 123–128.

Bean, C.J., 1996. On the cause of 1/f-power spectral scaling in borehole sonic logs. Geophysical Research Letters 23 (22), 3119–3122.

Bean, C., Marsan, D., Martini, F., 1999. Statistical measures of crustal heterogeneity from reflection seismic data: the role of seismic bandwidth. Geophysical Research Letters 26, 3241–3244.

Bellefleur, G., Malehmir, A., Müller, C., 2012. Elastic finite-difference modeling of volcanic-hosted massive sulphide deposits: a case study from Halfmile Lake, New Brunswick, Canada. Geophysics 77 (5), WC25–WC36. http://dx.doi.org/10.1190/GEO2011-0445.1.

Berkovitch, A., Belfer, I., Hassin, Y., Landa, E., 2009. Diffraction imaging by multifocusing. Geophysics 74, WCA75–WCA81.

Bohlen, T., Muller, C., Milkereit, B., 2003. Elastic seismic-wave scattering in massive sulphide orebodies: on the role of composition and shape. In: Eaton, D.W., Milkereit, B., Salisbury, M.H. (Eds.), Hardrock Seismic Exploration. Society of Exploration Geophysicists, pp. 70–89.

Bongajum, E., Milkereit, B., Adam, E., Meng, Y., 2012. Seismic imaging in hardrock environments: the role of heterogeneity? Tectonophysics 572–573, 7–15. http://dx.doi.org/10.1016/j.tecto.2012.03.003.

Carpentier, S.F.A., Roy-Chowdhury, K., 2009. Conservation of lateral stochastic structure of a medium in its simulated seismic response. Journal of Geophysical Research 114, B10314. http://dx.doi.org/10.1029/2008JB006123.

Cheraghi, S., Malehmir, A., Bellefleur, G., 2011. Crustal-scale reflection seismic investigations in the Bathurst Mining Camp, New Brunswick, Canada. Tectonophysics 506, 55–72. http://dx.doi.org/10.1016/j.tecto.2011.04.011.

Cheraghi, S., Malehmir, A., Bellefleur, G., 2012. 3D imaging challenges in steeply dipping mining structures: new lights on acquisition geometry and processing from the Brunswick No. 6 seismic data, Canada. Geophysics 77 (5), WC109–WC122. http://dx.doi.org/10.1190/GEO2011-0475.1.

Dehghannejad, M., Juhlin, C., Malehmir, A., Skyttä, P., Weihed, P., 2010. Reflection seismic imaging of the upper crust in the Kristineberg mining area, northern Sweden. Journal of Applied Geophysics 71, 125–136. http://dx.doi.org/10.1016/j.jappgeo.2010.06.002.

Dehghannejad, M., Malehmir, A., Juhlin, C., Skyttä, P., 2012. 3D constraints and finite-difference modeling of massive sulphide deposits: the Kristineberg seismic lines revisited, northern Sweden. Geophysics 77 (5), WC69–WC79. http://dx.doi.org/10.1190/GEO2011_0466.1.

Dell, S., Gajewski, D., 2011. Common-reflection-surface-based workflow for diffraction imaging. Geophysics 76, 5187–5195.

Dolan, S.S., Bean, C.J., 1997. Some remarks on the estimation of fractal scaling parameters from borehole wire-line logs. Geophysical Research Letters 24, 1271–1274.

Eaton, D.W., 1999. Weak elastic-wave scattering from massive sulphide orebodies. Geophysics 64, 289–299.

Ehsan, S.A., Malehmir, A., Dehghannejad, M., 2012. Re-processing and interpretation of 2D seismic data from the Kristineberg mining area, northern Sweden. Journal of Applied Geophysics 80, 43–55. http://dx.doi.org/10.1016/j.jappgeo.2012.01.004.

Flatté, S.M., Dashen, R., Munk, W.H., Watson, K.M., Zachriasen, F., 1979. Sound Transmission through a Fluctuating Ocean. Cambridge University Press, New York.

Frankel, A., Clayton, R.W., 1986. Finite difference simulation of seismic scattering: implications for the propagation of short-period seismic waves in the crust and models of crustal heterogeneity. Journal of Geophysical Research 91, 6465–6489.

Frenje, L., Juhlin, C., 2000. Scattering attenuation: 2D and 3D finite difference simulations vs. theory. Journal of Applied Geophysics 44, 33–46.

Goff, J.A., Holliger, K., 1994. Modal fields: a new method for characterization of random seismic velocity heterogeneity. Geophysical Research Letters 21 (6), 493–496.

Goff, J.A., Holliger, K., 1999. Nature and origin of upper crustal seismic velocity fluctuations and associated scaling properties: combined stochastic analysis of KTB velocity and lithology logs. Journal of Geophysical Research 104, 13169–13182.

Goff, J.A., Jordan, T.H., 1988. Stochastic modeling of sea floor morphology: inversion of sea beam data for second-order statistics. Journal of Geophysical Research 93, 13589–13608.

Goff, J.A., Levander, A., 1996. Incorporating 'sinuous connectivity' into stochastic models of crustal heterogeneity: examples from the Lewisian gneiss complex, Scotland, the Franciscan formation, California, and the Hafafit gneiss complex, Egypt. Journal of Geophysical Research 101, 8489–8502.

Gross, G.A., McLeod, C.R., 1980. A preliminary assessment of the chemical composition of iron formations in Canada. The Canadian Mineralogist 18, 223–229.

Holliger, K., 1996. Upper-crustal seismic velocity heterogeneity as derived from a variety of P-wave sonic logs. Geophysical Journal International 125, 813–829.

Holliger, K., 1997. Seismic scattering in the upper crystalline crust based on evidence from sonic logs. Geophysical Journal International 128, 65–72.

Holliger, K., Goff, J.A., 2003. A generic model for the 1/f-nature of seismic velocity fluctuations. In: Goff, J.A., Holliger, K. (Eds.), Heterogeneity in the Crust and Upper Mantle — Nature, Scaling, and Seismic Properties. Kluwer Academic/Plenum Scientific Publishers, New York, pp. 131–154.

Holliger, K., Levander, A., Goff, J.A., 1993. Stochastic modeling of the reflective lower crust: petrophysical and geological evidence from the Ivera Zone (Northern Italy). Journal of Geophysical Research 98, 11967–11980.

Holliger, K., Levander, A., Carbonell, R., Hobbs, R., 1994. Some attributes of wavefields scattered from Ivrea-type lower crust. Tectonophysics 232, 267–279.

Holliger, K., Green, A.G., Juhlin, C., 1996. Stochastic analysis of sonic logs from the upper crystalline crust: methodology. Tectonophysics 264, 341–356.

Hurich, C.A., 1996. Statistical description of seismic reflection wavefield: a step towards quantitative interpretation of deep seismic reflection profiles. Journal of Geophysical International 125, 719–728.

Hurich, C.A., Kocurko, A., 2000. Statistical approaches to interpretation of seismic reflection data. Tectonophysics 329, 251–267.

Juhlin, C., 1995. Finite difference elastic wave propagation in 2-D heterogeneous transversely isotropic media. Geophysical Prospecting 43 (6), 843–858. http://dx.doi.org/10.1111/gpr.1995.43.

Khaidukov, V., Landa, E., Moser, T.J., 2004. Diffraction imaging by focusing-defocusing: an outlook on seismic super resolution. Geophysics 69, 1478–1490.

Kneib, G., 1995. The statistical nature of the upper continental crystalline crust derived from in situ seismic measurements. Geophysical Journal International 122, 594–616.

Korn, M., 1993. Seismic waves in random media. Journal of Applied Geophysics 29, 247–269.

L'Heureux, E., Milkereit, B., Vasudevan, K., 2009. Heterogeneity and seismic scattering in exploration environments. Tectonophysics 472, 264–272.

Lentz, D.R., McCutcheon, S.R., 2006. The Brunswick No. 6 massive sulphide deposit, Bathurst Mining Camp, northern New Brunswick, Canada: a synopsis of the geology and hydrothermal alteration system. Exploration and Mining Geology 15, 1–34.

Levander, A., England, R.W., Smith, S.K., Hobbs, R.W., Goff, J.A., Holliger, K., 1994. Stochastic characterization and seismic response of upper and middle crustal rocks based on the Lewisian gneiss complex, Scotland. Geophysical Journal International 119, 243–259.

Line, C.E.R., Hobbs, R.W., Snyder, D.B., 1998. Estimation of upper-crustal heterogeneity in the Baltic Shield from seismic scattering and borehole logs. Tectonophysics 286, 171–183.

Luff, W.M., 1995. A history of mining in the Bathurst area, northern New Brunswick, Canada. The Canadian Institute of Mining, Metallurgy and Petroleum Bulletin 88, 63–68.
Malehmir, A., Bellefleur, G., 2009. 3D seismic reflection imaging of volcanic-hosted massive sulphide deposits: insights from re-processing Halfmile Lake data, New Brunswick, Canada. Geophysics 74, B209–B219. http://dx.doi.org/10.1190/1.3230495.
Malehmir, A., Bellefleur, G., 2010. Reflection seismic imaging and physical properties of base-metal and associated iron deposits in the Bathurst Mining Camp, New Brunswick, Canada. Ore Geology Reviews 38, 319–333.
Malehmir, A., Juhlin, C., 2010. An investigation of the effects of the choice of stacking velocities on residual statics for hardrock reflection seismic processing. Journal of Applied Geophysics 72, 28–38. http://dx.doi.org/10.1016/j.jappgeo.2010.06.008.
Malehmir, A., Schmelzbach, C., Bongajum, E., Bellefleur, G., Juhlin, C., Tryggvason, A., 2009. 3D constraints on a possible deep > 2.5 km massive sulphide mineralization from 2D crooked-line seismic reflection data in the Kristineberg mining area, northern Sweden. Tectonophysics 479, 223–240. http://dx.doi.org/10.1016/j.tecto.2009.08.013.
Malehmir, A., Dahlin, P., Lundberg, E., Juhlin, C., Sjöström, H., Högdahl, K., 2011. Reflection seismic investigations in the Dannemora area, central Sweden: insights into the geometry of poly-phase deformation zones and magnetite-skarn deposits. Journal of Geophysical Research 116, B11307. http://dx.doi.org/10.1029/2011JB008643.
Malehmir, A., Durrheim, R., Bellefleur, G., Urosevic, M., Juhlin, C., White, D., Milkereit, B., Campbell, G., 2012. Seismic methods in mineral exploration and mine planning: a general overview of past and present case histories and a look into the future. Geophysics 77 (5), WC173–WC190. http://dx.doi.org/10.1191/GEO2012-0028.1.
Malehmir, A., Andersson, M., Lebedev, M., Urosevic, M., Mikhaltsevitch, V., 2013. Experimental estimation of velocities and anisotropy of a series of Swedish crystalline rocks and ores. Geophysical Prospecting 61, 153–167. http://dx.doi.org/10.1111/j.1365-2478.2012.01063.x.
Malinowski, M., Schetselaar, E., White, D., 2012. 3D seismic imaging in the Flin Flon VMS mining camp — part II: forward modeling. Geophysics 77 (5), WC81–WC93. http://dx.doi.org/10.1190/GEO2011-0474.1.
Marsan, D., Bean, C.J., 1999. Multiscaling nature of sonic velocities and lithology in the upper crystalline crust: evidence from the KTB main borehole. Geophysical Research Letters 26, 275–278.
Milkereit, B., Eaton, D., 1998. Imaging and interpreting the shallow crystalline crust. Tectonophysics 286, 5–18.
Milkereit, B., Eaton, D.W., Wu, J., Perron, G., Salisbury, M.H., Berrer, E., Morrison, G., 1996. Seismic imaging of massive sulphide deposits: part II. Reflection seismic profiling. Economic Geology 91, 829–834.
Milkereit, B., Berrer, E.K., King, A.R., Watts, A.H., Roberts, B., Adam, E., Eaton, D.W., Wu, J., Salisbury, M.H., 2000. Development of 3-D seismic exploration technology for deep nickel–copper deposits—a case history from the Sudbury basin, Canada. Geophysics 65, 1890–1899.
Muller, G., Roth, M., Korn, M., 1992. Seismic-wave traveltimes in random media. Geophysical Journal International 110, 29–41.
Mwenifumbo, C.J., Salisbury, M., Elliott, B.E., Pflug, K.A., 2005. Use of multichannel gamma–gamma logs to improve the accuracy of log-derived densities of massive sulfides. Petrophysics 46, 346–353.
Pilkington, M., Todoeschuck, J.P., 2004. Power-law scaling behavior of crustal density and gravity. Geophysical Research Letters 31, L09606. http://dx.doi.org/10.1029/2004GL019883.
Poppeliers, C., 2007. Estimating vertical stochastic scale parameters from seismic reflection data: deconvolution with non-white reflectivity. Journal of Geophysical International 168, 769–778.
Pretorius, C.C., Muller, M.R., Larroque, M., Wilkins, C., 2003. A review of 16 years of hardrock seismics on the Kaapvaal Craton. In: Eaton, D.W., Milkereit, B., Salisbury, M.H. (Eds.), Hardrock Seismic Exploration. Society of Exploration Geophysicists, pp. 247–268.
Priestly, M.B., 1981. Spectral Analysis and Time Series. Academic Press, San Diego, California.
Pullammanappallil, S., Levander, A., Larkin, S., 1997. Estimation of crustal stochastic parameters from seismic exploration data. Journal of Geophysical Research 102, 269–286.
Rogers, N., van Staal, C.R., 1997. Comparing the Bathurst Mining Camp to the Japan Sea and Okinawa Trough: ancient, recent, and active back-arcs [abs.]. Geological Association of Canada-Mineralogical Association of Canada, Annual Meeting, 22, A-127.
Rogers, N., van Staal, C.R., Winchester, J.A., Fyffe, L.R., 2003. Provenance and chemical stratigraphy of the sedimentary rocks of the Miramichi, Tetagouche, California Lake and Fournier groups, northern New Brunswick. In: Goodfellow, W.D., McCutcheon, S.R., Peter, J.M. (Eds.), Massive Sulphide Deposits of the Bathurst Mining Camp, New Brunswick, and Northern Maine: Economic Geology, Monograph, 11, pp. 111–128.
Roth, M., Korn, M., 1993. Single scattering theory versus numerical modeling in 2D random media. Geophysical Journal International 112, 124–140.
Salisbury, M.H., Harvey, C.W., Matthews, L., 2003. The acoustic properties of ores and host rocks in hardrock terranes. In: Eaton, D.W., Milkereit, B., Salisbury, M.H. (Eds.), Hard Rock Seismic Exploration. Society of Exploration Geophysicists, pp. 9–19.
van Staal, C.R., 1987. Tectonic setting of the Tetagouche group in northern New Brunswick: implications for plate tectonic models of the northern Appalachians. Canadian Journal of Earth Sciences 24, 1329–1351.
van Staal, C.R., 1994. Brunswick subduction complex in the Canadian Appalachians: record of the Late Ordovician to Late Silurian collision between Laurentia and the Gander margin of Avalon. Tectonics 13, 946–962.
van Staal, C.R., Wilson, R.A., Rogers, N., Fyffe, L.R., Langton, J.P., McCutcheon, S.R., McNicoll, V., Ravenhurst, C.E., 2003. Geology and tectonic history of the Bathurst Supergroup, Bathurst Mining Camp and its relationships to coeval rocks in southwestern New Brunswick and adjacent Maine—a synthesis. In: Goodfellow, W.D., McCutcheon, S.R., Peter, J.M. (Eds.), Massive Sulphide Deposits of the Bathurst Mining Camp, New Brunswick, and Northern Maine: Economic Geology Monograph, 11, pp. 37–60.
von Karman, T., 1948. Progress in the statistical theory of turbulence. Journal of Marine Research 7, 252–264.
Whalen, J.B., Rogers, N., van Staal, C.R., Longstaffe, F.J., Jenner, G.A., Winchester, J.A., 1998. Geochemical and isotopic (Nd, O) data from the Ordovician felsic plutonic and volcanic rocks of the Miramichi Highlands: petrogenetic and metallogenic implications for the Bathurst Mining Camp. Canadian Journal of Earth Sciences 35, 237–252.
White, D.J., Secord, D., Malinowski, M., 2012. 3D seismic imaging of volcanogenic massive sulfide deposits in the Flin Flon mining camp, Canada: part 1 — seismic results. Geophysics 77 (5), WC47–WC58. http://dx.doi.org/10.1190/GEO2011-0487.1.
Wills, A.O., Lentz, D.R., Roy, G., 2006. Chemostratigraphy at the Brunswick No. 6 volcanic-sediment-hosted massive sulphide deposit, New Brunswick: resolving geometry from drill core in deformed felsic volcanic rocks. Exploration and Mining Geology 15, 35–51.
Wu, R.S., 1989. Seismic wave scattering. In: James, D. (Ed.), Encyclopedia of Geophysics. Van Nostrand Reinhold, New York, pp. 1166–1187.
Wu, R.S., Aki, K., 1985a. The fractal nature of the inhomogeneities in the lithosphere evidenced from seismic wave scattering. Pure and Applied Geophysics 123, 805–818.
Wu, R.S., Aki, K., 1985b. Scattering characteristics of elastic waves by an elastic heterogeneity. Geophysics 50, 582–595.
Wu, R.S., Aki, K., 1988. Introduction: seismic wave scattering in three-dimensionally heterogeneous Earth. Pure and Applied Geophysics 128, 1–6.
Wu, R.S., Xu, Z., Li, X.P., 1994. Heterogeneity spectrum and scale-anisotropy in the upper crust revealed by the German Continental Deep-Drilling (KTB) Holes. Geophysical Research Letters 21, 911–914.